

Design, synthesis, in silico studies, and biological evaluation of N4-acetyl/benzoyl piperazinyl ciprofloxacin–amino acid conjugates as

Downloaded from: https://research.chalmers.se, 2026-11-23 15:59 UTC

Citation for the original published paper (version of record):
El-sagheir, A., Sidarta, M., Bunker, A. et al (2027). Design, synthesis, in silico studies, and biological evaluation of N4-acetyl/benzoyl
piperazinyl ciprofloxacin–amino acid conjugates as broad-spectrum antimicrobial agents. European Journal of Pharmaceutical Sciences, 228. http://dx.doi.org/10.1016/j.ejps.2026.107704

N.B. When citing this work, cite the original published paper.

research.chalmers.se offers the possibility of retrieving research publications produced at Chalmers University of Technology. It covers all kind of research output: articles, dissertations, conference papers, reports etc. since 2004. research.chalmers.se is administrated and maintained by Chalmers Library

(article starts on next page)

European Journal of Pharmaceutical Sciences 228 (2027) 107704

Contents lists available at ScienceDirect

European Journal of Pharmaceutical Sciences

journal homepage: www.elsevier.com/locate/ejps

Design, synthesis, *in silico* studies, and biological evaluation of N^4-acetyl/benzoyl piperazinyl ciprofloxacin–amino acid conjugates as broad-spectrum antimicrobial agents

Ahmed M.Kamal El-sagheir [a,b], Margareth Sidarta [c,d], Alex Bunker [e], Michaela Wenzel [c,d,*], Jari Yli-Kauhaluoma [a,*]

[a] Drug Research Program, Division of Pharmaceutical Chemistry and Technology, Faculty of Pharmacy, University of Helsinki, FI-00014 Helsinki, Finland
[b] Medicinal Chemistry Department, Faculty of Pharmacy, Assiut University, Assiut, 71526, Egypt
[c] Division of Molecular Bioscience, Department of Life Sciences, Chalmers University of Technology, 412 96 Gothenburg, Sweden
[d] Center for Antibiotic Resistance Research in Gothenburg (CARe), 413 46 Gothenburg, Sweden
[e] Drug Research Program, Division of Pharmaceutical Biosciences, Faculty of Pharmacy, University of Helsinki, FI-00014 Helsinki, Finland

ARTICLE INFO

Keywords:
Ciprofloxacin conjugates
Molecular hybridization
Broad-spectrum
Antimicrobial
Antibiofilm

ABSTRACT

This study reports a second-stage optimization of our previously reported ciprofloxacin derivatives through molecular hybridization, with structural modifications aimed at improving antimicrobial potency and activity against resistant strains. Their structures and identities were confirmed by spectroscopic techniques, elemental analysis, and HPLC. *In vitro* antimicrobial activity showed enhanced potency across a panel of bacterial strains. The derivatives demonstrated promising activity against both wild-type and resistant strains, while the most active derivatives also exhibited promising antimycobacterial activity. The most active compounds were selected for further *in vitro* and live-cell mode-of-action studies. Several compounds showed biofilm-inhibiting activity against *Staphylococcus aureus* at sub-MIC. Phenotypic mode-of-action studies indicated topoisomerase inhibition in both *E. coli* and *Bacillus subtilis*. Enzyme inhibition studies revealed potent activity against DNA gyrase and topoisomerase IV. Additionally, the best anti-*Helicobacter pylori* candidates showed promising urease inhibition. Selected derivatives showed bactericidal activity with minimal resistance development compared with ciprofloxacin. The cytotoxicity study indicated low *in vitro* cytotoxicity under the tested conditions. Molecular modeling supported favorable binding and inhibitory potential, while QSAR linked physicochemical properties to biological activity, providing mechanistic insights and guiding compound optimization toward improved efficacy and development. Overall, the synthesized ciprofloxacin hybrids showed promising antimicrobial activity and potential to combat bacterial resistance.

1. Introduction

Quinolones are synthetic antibacterials used to treat serious infectious diseases. Their therapeutic usage is limited due to low efficacy against Gram-positive bacteria, and a propensity for resistance development. Newer generations of fluoroquinolones (FQs) have tackled many of these obstacles, showing notable improvements of their antimicrobial spectrum (Panigrahi et al., 2024). These advances have contributed to the escalating clinical use of FQs (Naeem et al., 2016; Bisacchi, 2015). Given these clinical merits, it is critical to understand how FQs exert their antibacterial effects on the cellular and molecular level.

DNA gyrase and topoisomerase IV are two crucial bacterial enzymes involved in DNA synthesis and repair. DNA gyrase is the main target of FQs in Gram-negative bacteria, as well as *Mycobacterium tuberculosis*, whereas topoisomerase IV is the major target in Gram-positive bacteria. When DNA gyrase and topoisomerase IV are inhibited, the topoisomerase–DNA complex is trapped, which interferes with DNA replication, induces DNA strand breaks, and ultimately leads to cell death (Drlica and Zhao, 2021).

Due to their superior bioavailability and broad antibacterial spectrum, FQs have advanced to considerable importance in the treatment of bacterial infections. However, their extensive clinical use has been associated with a steady rise in quinolone resistance. The most common

* Corresponding authors.
E-mail addresses: wenzelm@chalmers.se (M. Wenzel), jari.yli-kauhaluoma@helsinki.fi (J. Yli-Kauhaluoma).

https://doi.org/10.1016/j.ejps.2026.107704
Received 14 August 2026; Received in revised form 27 October 2026; Accepted 30 October 2026
Available online 2 November 2026
0928-0987/© 2026 The Author(s). Published by Elsevier B.V. This is an open access article under the CC BY license (http://creativecommons.org/licenses/by/4.0/).

resistance mechanisms involve mutations in the *gyrA* and *parC* genes, which encode the A subunits of DNA gyrase and topoisomerase IV, respectively (Millanao et al., 2021). These mutations lead to amino acid substitutions which alter the enzyme structure and decrease drug binding (Correia et al., 2017). Other mechanisms involve overexpression of active efflux pumps and decreased membrane permeability, reducing intracellular drug concentration (Yanat et al., 2017). Consequently, significant endeavors have been undertaken to modify FQs with the aim to overcome multi-drug resistance.

Structure–activity relationship (SAR) studies of FQs have established that the 4-oxo-1,4-dihydroquinoline-3-carboxylic skeleton is an essential pharmacophore for DNA gyrase inhibition (Fàbrega et al., 2009). The 6-fluoro substituent generally enhances antibacterial activity (Singh et al., 2015). Substitution at the C-7 position, particularly with a piperazine ring, plays an important role in modulating antibacterial activity, spectrum, and safety. The C-7 position is also considered a key site for accommodating bulky functional groups (Pham et al., 2019). Furthermore, the interaction of FQs with their target enzymes and their activity against resistant strains can be influenced by the C-7 substituent and modifications at the carboxyl group. Clinical development of FQs has involved systematic modification of key positions on the quinolone scaffold, including the N^4-piperazine substituent and carboxyl group, to optimize antibacterial activity, spectrum, pharmacokinetic properties, and tolerability (Wang et al., 2012; Abdullah et al., 2017; Mohamed et al., 2018). In experimental studies, further derivatization of these positions has been explored to introduce additional structural features and potentially enhance antibacterial and antimycobacterial activity.

Beyond drug resistance due to target mutations and efflux/uptake modifications, bacterial biofilm formation poses an additional therapeutic challenge. Biofilms are multicellular communities encased in a protective extracellular polymeric matrix composed of proteins, polysaccharides, and nucleic acids. Bacteria can use this polymeric matrix as a survival strategy to evade host defense mechanisms (Vestby et al., 2020). Biofilm-associated bacteria can exhibit markedly reduced antimicrobial susceptibility compared with planktonic cells, contributing to persistent and difficult-to-treat infections (Opoku-Temeng and Sintim, 2017). Suppressing biofilm production can increase antibiotic sensitivity without necessarily affecting bacterial growth, potentially exerting less selection pressure than traditional antibiotic therapy and making antibiofilm strategies increasingly appealing (Fong et al., 2019). Many FQ derivatives with antibiofilm activity have been reported, providing an additional target with high potential against resistant bacteria (Marc et al., 2019; Fedorowicz et al., 2023).

This work represents a focused second-stage optimization of ciprofloxacin-based hybrids, building on our previous efforts in the rational design of FQ derivatives (Kamal El-sagheir et al., 2026) and established SAR findings for FQs (Kamal El-sagheir et al., 2023a; Kamal El-sagheir et al., 2023b; Kamal El-sagheir et al., 2023c). In our previous study, we mainly explored ester, hydrazide, hydroxamic acid, and oxadiazole derivatives, which demonstrated the potential of ciprofloxacin hybridization while highlighting the need for further structural diversification. In the present work, we therefore investigated a distinct set of structural modifications aimed at further optimizing antimicrobial activity and exploring structure–activity relationships. Specifically, we examined N^4-acetyl/benzoyl substitution on the piperazine moiety, incorporation of glycine or serine amino acid linkers, and integration of diverse bioactive scaffolds, including thiosemicarbazide, aldehyde hydrazones, isatins, cyclic imides, tetrazole, and thiazolidinone (Fig. 1). Glycine and serine were selected to modulate polarity and hydrogen-bonding capacity, while acetyl and benzoyl groups were introduced to vary steric and lipophilic properties. The selected heterocyclic scaffolds were incorporated to provide additional structural and interaction possibilities. Collectively, these modifications were designed to systematically vary the hydrophobic, electronic, and topological properties of the ciprofloxacin hybrids and examine their effects on antimicrobial activity, particularly against drug-resistant bacteria.

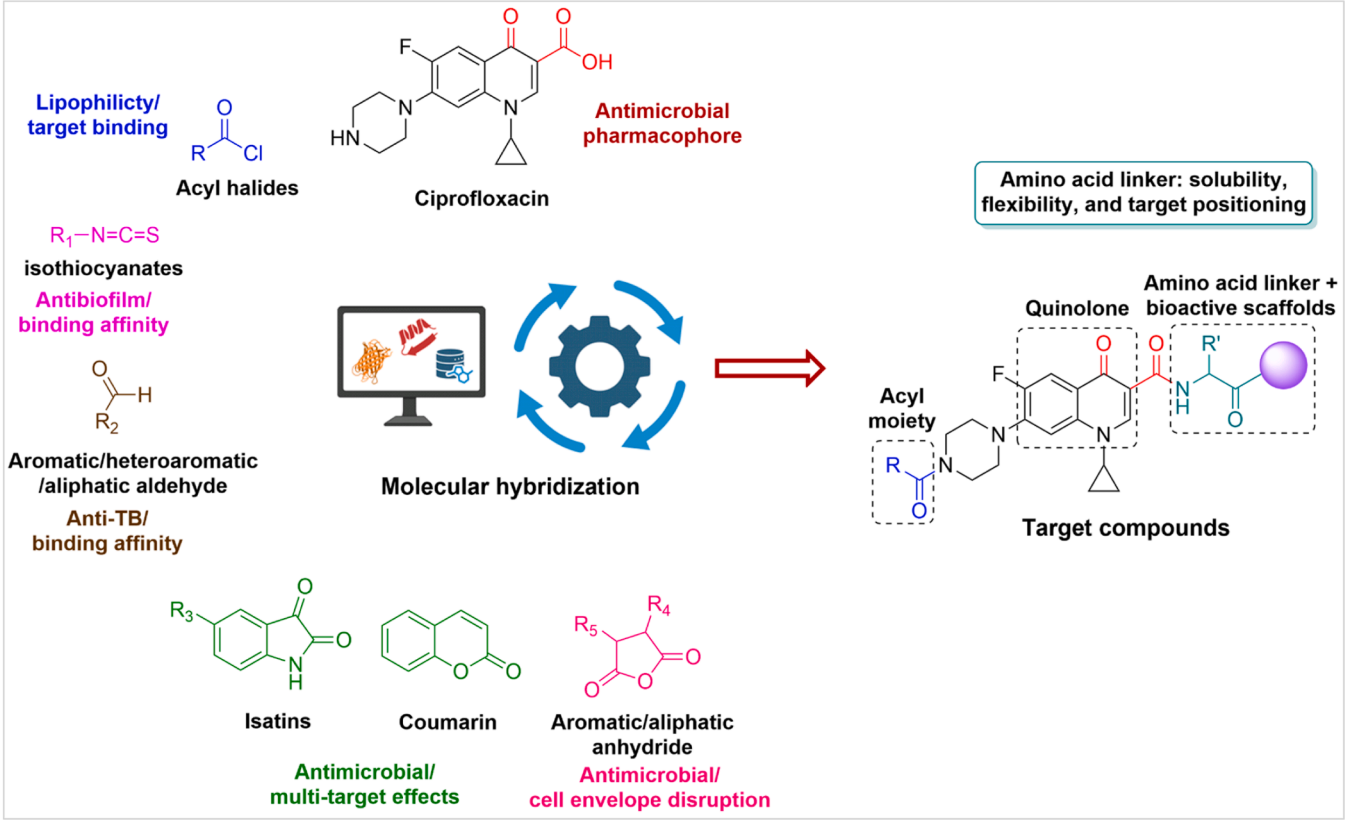

Fig. 1. Design rationale and strategy for the target compounds.

The modifications may also influence molecular properties related to bacterial penetration, efflux, and target interactions, while the amino acid linkers and appended heterocyclic groups may contribute to changes in biofilm-associated activity. Molecular modeling was used to provide supportive insights into these design considerations and potential ligand–target interactions. Thus, the present study extends our previous work through a second stage of structural diversification and systematic evaluation of the resulting effects on antimicrobial activity, resistance-related properties, and biofilm formation. The novelty of the present study lies in this expanded structural diversification and the comparative evaluation of how these modifications influence the antimicrobial properties of ciprofloxacin conjugates.

2. Results and discussion

2.1. Chemistry

The synthetic methods utilized for preparation of the target derivatives are depicted in Schemes 1–4. The structures of all derivatives were confirmed using spectroscopic and analytical techniques, including ^{1}H NMR, ^{13}C NMR, ^{19}F NMR, MS, and elemental analysis (with values within ±0.3% of the theoretical values). Routine assessment of the compounds also included thin-layer chromatography (TLC) and melting point determination. In addition, HPLC analysis was performed for selected lead compounds (8a, 14d, 15b, 15e, 17b, 19k, 20e, 23i, and 24b), confirming chromatographic purity above 95% for these compounds. The *in vitro* stability of the lead compounds, particularly those with imine bonds, was confirmed under physiological conditions (pH 7.4, 37 °C) over 14 days, with HPLC showing ≥97% of the parent peak retained, supporting the reliability of the observed biological activity (full characterization: Fig. S1–S207, Table S1, Section S7.2).

The synthesized derivatives represent an extension of our previously published work (Kamal El-sagheir et al., 2026); accordingly, the compound numbering has been continued from the previously reported series (3–13a-f and 8′–9′a-f). Scheme 1 outlines the synthesis of *N*-acetyl and benzoyl ciprofloxacin derivatives 3a and 3b in the yield of 97–99% as reported in the literature (Ji et al., 2015; Struga et al., 2023). Next, glycine/serine amino acid esters (6a, 74% yield; 6b, 86% yield; 7a, 74% yield) and hydrazide derivatives (8a, 94% yield; 8b, 96% yield; 9a, 77% yield) were synthesized and fully characterized as described in our previous work (Kamal El-sagheir et al., 2026). These hydrazide intermediates were employed as building blocks for the synthesis of subsequent derivatives explored in this study. The substituted thiosemicarbazide derivatives 14, 18 and 22a-d were synthesized by reacting hydrazides 8a, 8b and 9a with substituted isothiocyanate in ethanol under reflux (Scheme 1). The resulting compounds were recrystallized from 2-propanol (ethanol, in case of serine derivatives) to afford the desired thiosemicarbazides in 59–79% yields.

Scheme 2 outlines the synthesis of various hydrazones (15, 19a-o, 23a-q) via the condensation of hydrazides (8a, 8b and 9a) with a variety of aromatic, heteroaromatic, and aliphatic aldehydes. The reaction was catalyzed by glacial acetic acid, except for compounds 15h, 15l, 15m, 15o, 19h, 19l, 19m, 19o, 23k, 23p and 23q, which used *p*-toluenesulfonic acid as a catalyst. Methanol was the solvent of choice, except for 23n and 23o, where THF was used instead. The hydrazones were purified by recrystallization using DMF/water, except for serine derivatives, which were recrystallized from ethanol. Notably, compounds 23h and 23n-q were recrystallized from acetonitrile. The final yields of the purified hydrazones ranged from 61% to 83%. It is noteworthy that isolated hydrazones exist as a mixture of *E/Z* geometrical isomers (*ca.* 3:1 in case of glycine, *ca.* 1:1 in case of serine) around the double bond (-N═CH-). This was evidenced by the presence of duplicate sets of peaks

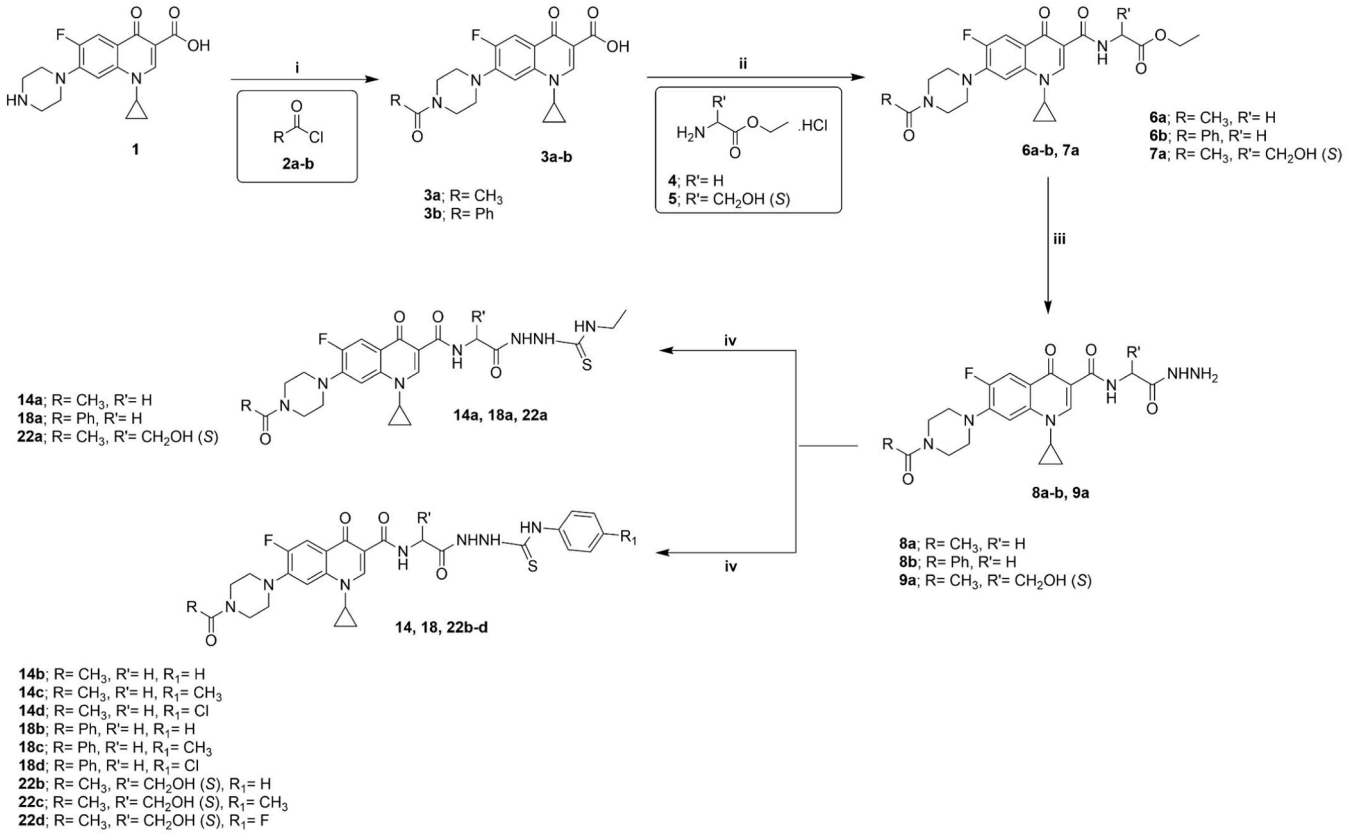

Scheme 1. Synthesis of the target derivatives 3–8a/8b, 9a, 14, 18, and 22a-d. Reagents and conditions: (i) Et_3N, THF, reflux, 6 h; (ii) ClCOOEt, Et_3N, DCM, rt, 24 h; (iii) $H_2NNH_2{\cdot}H_2O$, MeOH, reflux, 8–12 h; (iv) R_1NCS, MeOH, reflux, 5–8 h.

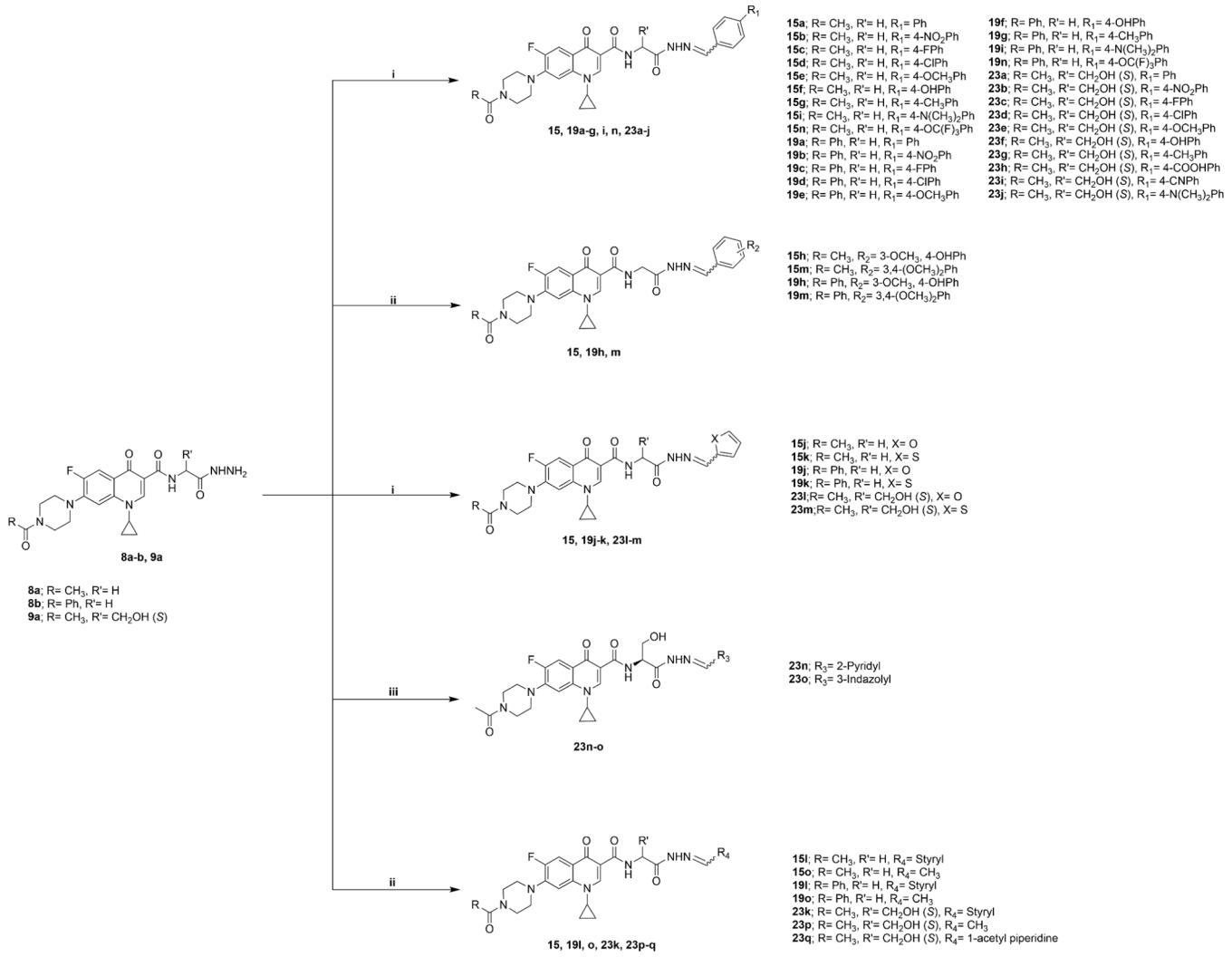

Scheme 2. Synthesis of the target derivatives 15, 19a-o, and 23a-q. Reagents and conditions: (i) Aromatic/heteroaromatic aldehyde, MeOH, CH_3COOH, reflux, 4–8 h; (ii) Disubstituted benzaldehyde/aliphatic aldehyde, MeOH, PTSA, reflux, 5–8 h; (iii) Heteroaromatic aldehyde, THF, CH_3COOH, reflux, 6 h.

for certain signals such as azomethine (N═CH) and hydrazide (HNN═C) protons. Generally, the protons in the *Z*-isomer are more de-shielded by 0.2–0.8 ppm compared to the *E*-isomer, due to their closer proximity to the hydrazide group. Chemical shifts are significantly influenced by the molecular configuration, as further confirmed by predicted chemical shifts from density functional theory (DFT) calculations (Table S2). Additionally, DFT findings indicate that *Z*-isomers exhibit higher electronegativity than *E*-isomers, which contributes to the greater de-shielding observed in *Z*-isomers. The ratio of *E/Z* isomers was determined through chemical shift analysis and integration of the azomethine proton (-N═CH-) as well as aromatic protons. The *E*-isomer was the predominant form. DFT calculations revealed that the *E*-isomer had lower total energy, making it more stable and thermodynamically favorable than the *Z*-isomer. This observation is consistent with previously reported data in the literature (Abdelgawad et al., 2022; Fernández-Palacios et al., 2023). The isomeric mixture appeared as a single spot on thin-layer chromatography (TLC), suggesting minimal polarity differences and rapid interconversion. Therefore, chromatographic separation was impractical under standard conditions, and HPLC analysis similarly showed a single chromatographic peak or overlapping peaks. As the *E*-isomer is thermodynamically favored and dominates the equilibrium mixture, biological evaluation was conducted using the mixture, aligned with early-stage screening practices.

To further expand the structural diversity of the series, the hydrazide intermediates were coupled with privileged isatin motifs. Ciprofloxacin-isatin hybrid derivatives 16, 20, and 24a-e were prepared via condensation of various isatins with hydrazides 8a, 8b, and 9a in methanol, using glacial acetic acid as a catalyst under reflux (Scheme 3). The products were purified by recrystallization from 1,4-dioxane/water (THF, in case of serine derivatives), giving the desired compounds in 64–89% yields. Isatin Schiff bases were isolated as a mixture of *E/Z* geometrical isomers (*ca.* 2:3) around the double bond (-N═C-isatin), favoring the *Z*-isomer. The isomeric ratio was inferred by chemical shift analysis and integration of isatin proton signals. Notably, no consistent behavior was observed across all compounds in shielding or de-shielding between *E* and *Z* isomers. This variability highlighted the benefit of DFT calculations, which were employed to predict and assign the NMR chemical shifts of both isomers more confidently (Table S2). Moreover, DFT calculations indicated that the *Z*-isomer has lower total energy than the *E*-isomer, rendering it more stable and thermodynamically favored. This observation was in line with previous findings in the literature (Abd El-wahab et al., 2022; Qayed et al., 2022).

In addition to the isatin-containing hybrids, the coumarin hybrid derivative 25 was synthesized by reacting coumarin-6-carbaldehyde with hydrazide derivative 9a in ethanol, using glacial acetic acid as a catalyst (Scheme 3). The resulting product was purified by recrystallization from a DMF/water mixture, giving the desired compound with a 77% yield. The reaction between hydrazides 8a, 8b and 9a and different

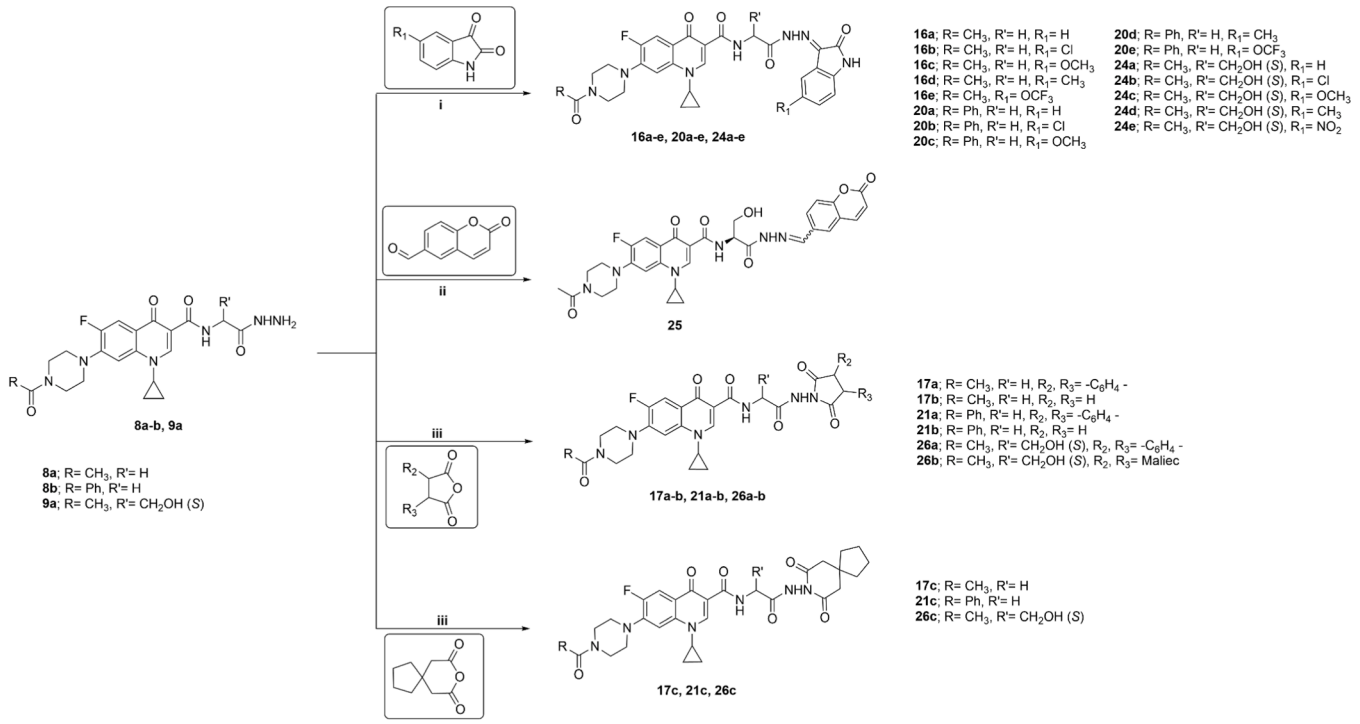

Scheme 3. Synthesis of the target derivatives 16a-e, 17a-c, 20a-e, 21a-c, 24a-e, 25, and 26a-c. Reagents and conditions: (i) MeOH, CH_3COOH, reflux, 8–12 h; (ii) EtOH, CH_3COOH, reflux, 5 h; (iii) CH_3COOH, sonication, 70 °C, 4–6 h.

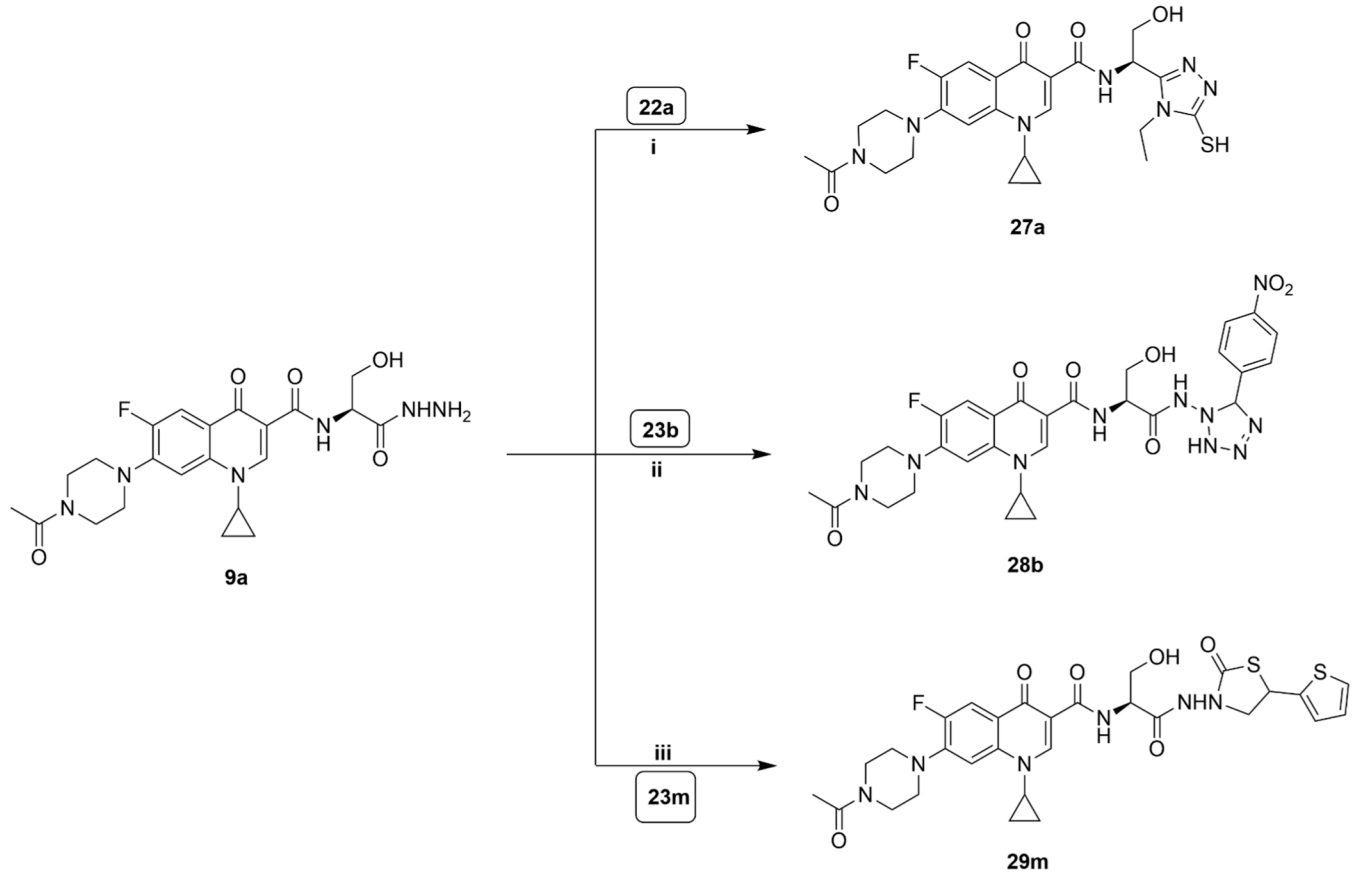

Scheme 4. Synthesis of the target derivatives 27a, 28b, and 29m. Reagents and conditions: (i) 1. KOH, MeOH, reflux, 10 h, 2. 10% HCl in H_2O; (ii) NaN_3, MeOH, MW, 60 °C, 5 h; (iii) $HSCH_2COOH$, MW, 70 °C, 3 h.

cyclic anhydrides in glacial acetic acid under sonication produced cyclic imide derivatives 17, 21, 26a-c (Scheme 3). The imide compounds were purified by recrystallization from ethanol in yields ranging from 65% to 74%.

Finally, selected thiosemicarbazide and hydrazone derivatives were further transformed into heterocyclic systems. The triazole thiol derivative 27a was synthesized via cyclization of thiosemicarbazide 22a under alkaline catalysis in methanol (Scheme 4). The resulting triazole product was purified by recrystallization from ethyl acetate, yielding the desired compound with a 53% yield. The 2,5-dihydro-1*H*-tetrazole derivative 28b was obtained by reacting hydrazone 23b with sodium azide in methanol under microwave irradiation at 60 °C (Scheme 4). Recrystallization from ethanol gave the product in 90% yield. The thiazolidine derivative 29m was similarly prepared from hydrazone 23m and thioglycolic acid in acetic acid under microwave irradiation at 70 °C, giving a 62% yield after recrystallization from acetonitrile.

2.2. Biological investigation

2.2.1. In vitro antimicrobial activity

The minimal inhibitory concentrations (MICs) of the compounds were determined against *E. coli* ATCC 8739, *Pseudomonas aeruginosa* ATCC 27,853, and *Klebsiella pneumoniae* ATCC 10,031 as Gram-negative wild-type strains; *Staphylococcus aureus* ATCC 6538 and *Enterococcus faecalis* ATCC 19,433 as Gram-positive wild-type strains; and *Helicobacter pylori* ATCC 700,392 as a microaerophilic Gram-negative strain. Moreover, multidrug-resistant (MDR) strains were evaluated, including methicillin-resistant *S. aureus* ATCC 43,300 (MRSA; resistant to β-lactam antibiotics and fluoroquinolones) and *E. coli* NCTC 13,476 (clinical isolate; resistant to third-generation cephalosporins and fluoroquinolones). Antimycobacterial activity was determined against *M. tuberculosis* MC26020 (attenuated strain). All assays were performed in triplicate using the broth microdilution method adapted from CLSI guidelines (Clinical and Laboratory Standards Institute 2013; Kadeřábková et al., 2024). Ciprofloxacin (**CIP**), isoniazid (**INH**), and nitazoxanide (**NTZ**) were used as reference drugs (Table S3). In accordance with EUCAST clinical breakpoints for ciprofloxacin (http s://www.eucast.org/clinical_breakpoints) and commonly applied hit-selection criteria in antibacterial drug discovery, the antimicrobial activity of the synthesized compounds was evaluated. Compounds were considered "hits" if they exhibited MIC values equal to or lower than ciprofloxacin against wild-type strains, and ≤5–20 μM against resistant strains, indicating meaningful activity suitable for further optimization.

Within the Gram-negative test panel, several of the investigated compounds demonstrated promising activity against *E. coli*, with MIC values ranging from 0.25 to 0.45 μM, showing activity comparable to or modestly higher than ciprofloxacin (MIC 0.45 μM). Notably, the most active hybrid compounds, including 15b, 15j, 19d, 19k, 23i, and 27a, exhibited lower MIC values than their corresponding hydrazide intermediates 8a (MIC 0.45 μM), 8b (MIC 0.59 μM), and 9a (MIC 1.05 μM). *P. aeruginosa* displayed comparable susceptibility to the investigated compounds (MIC 1.32–2.21 μM) and ciprofloxacin (MIC 2.26 μM). The most promising candidates 15d, 16b, 18d, and 23b also showed lower MIC values than the hydrazide intermediates. Against *K. pneumoniae*, the newly synthesized compounds showed MIC values of 1.06–2.88 μM, indicating comparable to modestly improved activity relative to ciprofloxacin (MIC 3.02 μM). The highest activity was observed for compounds 15n, 19b, 20e, and 24e. Regarding MDR *E. coli*, some compounds retained moderate activity, with MIC values ranging from 4.25 to 18.10 μM. The most promising compounds included 14d, 15b, 20b, and 23i.

Among the Gram-positive panel, several compounds exhibited potent activity against *S. aureus*, with MIC values ranging from 0.47 to 2.22 μM, including compounds with lower MIC values than ciprofloxacin (MIC 2.26 μM). Interestingly, compounds 15e, 16a, and 25 showed prominent activity with MIC values below 1 μM. These compounds also demonstrated lower MIC values than the hydrazide intermediates. Against *E. faecalis*, the examined compounds exhibited MIC values of 1.58–3.62 μM, with several compounds showing MIC values lower than ciprofloxacin (MIC 3.77 μM). The most active compounds included 15i, 15m, 18b, and 24c. Against MRSA, the most active compounds showed MIC values of 3.55–15.98 μM, with several compounds showing lower MIC values than ciprofloxacin, with the best-performing compounds being 15e, 16a, 19f, 23e, and 25.

H. pylori was more susceptible to several of the new hybrid compounds (MIC 1.22–2.95 μM) compared with ciprofloxacin (MIC 3.02 μM) and nitazoxanide (MIC 13.01 μM). The observed differences should be interpreted cautiously given the expected variability of MIC measurements. Representative compounds from each series (14d, 15j, 19c, 22d, and 23h) exhibited lower MIC values than the hydrazide intermediates. With respect to *M. tuberculosis*, some investigated compounds displayed MIC values ranging from 1.30 to 2.21 μM. Compounds 15b, 16e, 19c, and 25 were as or slightly more active than ciprofloxacin (MIC 2.26 μM) and isoniazid (MIC = 1.82 μM) under the tested conditions. Overall, these findings support broad *in vitro* antibacterial activity across the tested panel; however, further studies using diverse clinical isolates are needed to establish broader therapeutic potential.

Overall, several of the new hybrid ciprofloxacin derivatives demonstrated enhanced antibacterial activity against selected strains. In some cases, their activities surpassed those of the reference drugs as well as the corresponding hydrazide intermediates. The influence of each structural modification on the observed improvements in antibacterial activity was addressed through a comprehensive structure-activity relationship (SAR) analysis, providing a framework for further optimization (Fig. 2). Thiosemicarbazide derivatives (14, 18, 22a–d) showed enhanced activity against Gram-negative bacteria, including *H. pylori* and *M. tuberculosis*, upon introduction of ethyl, phenyl, *p*-chloro, and *p*-fluorophenyl substituents. The *p*-chloro group showed the greatest effect, particularly against MDR *E. coli* (MIC 6.51–17.75 μM), indicating that this substituent was associated with increased Gram-negative activity. For Gram-positive bacteria, electron-donating groups such as ethyl, phenyl, and *p*-tolyl were most effective, with compound 18b showing a MIC of 9.35 μM against MRSA.

For the hydrazone series (15, 19, 23a–q), the highest activity against Gram-negative bacteria was observed with *p*-substituted phenyl rings bearing electron-withdrawing groups (NO_2 > F > COOH > CN > Cl > OCF_3). Heterocycles such as phenyl isosteres showed moderate activity, with five-membered rings (thiophene > furan > pyridine > indazole) generally being more active than six-membered or bicyclic rings. This was followed by *p*-substituted electron-donating phenyl rings, unsubstituted phenyl, styryl, and aliphatic substituents. Against *M. tuberculosis*, activity followed the order *p*-NO_2pH > *p*-FPh > *p*-COOHPh > *p*-OCF_3 > thiophene > *p*-ClPh > pyridine > furan, with the most active compounds against MDR *E. coli* showing MICs of 4.33–18.10 μM. Against Gram-positive bacteria, aromatic hydrazones were generally more active (*p*-OCH_3 > *p*-OH > *p*-COOH > *p*-$N(CH_3)_2$ > *p*-CH_3 > *m*-OH,*p*-OCH_3 > *m*,*p*-$(OCH_3)_2$ > *p*-NO_2 > *p*-F > *p*-Cl > thiophene), while aliphatic hydrazones followed CH_3 > acetylpiperidine > styryl. The strongest activity against MRSA (MIC 3.55–19.81 μM) was observed for *p*-substituted, electron-donating aromatic and aliphatic hydrazones. Activity was also observed for the hydrazone with a *p*-carboxy substituent (Fig. 2).

For the isatin hybrid derivatives, substituents at the 5-position strongly influenced activity against Gram-negative bacteria and *M. tuberculosis*, with potency increasing in the order OCF_3 > Cl > NO_2 > H > OCH_3 > CH_3, highlighting the association of electron-withdrawing groups with increased activity in this series. The compounds showed promising activity against MDR *E. coli* with MICs of 7.46–15.67 μM. For Gram-positive bacteria, the trend was reversed (H > CH_3 > OCH_3 > OCF_3 > Cl > NO_2), indicating higher activity for unsubstituted isatin and electron-donating groups (Fig. 2). The most active compounds against MDR MRSA exhibited MICs of 5.23–12.58 μM. The observed activity of

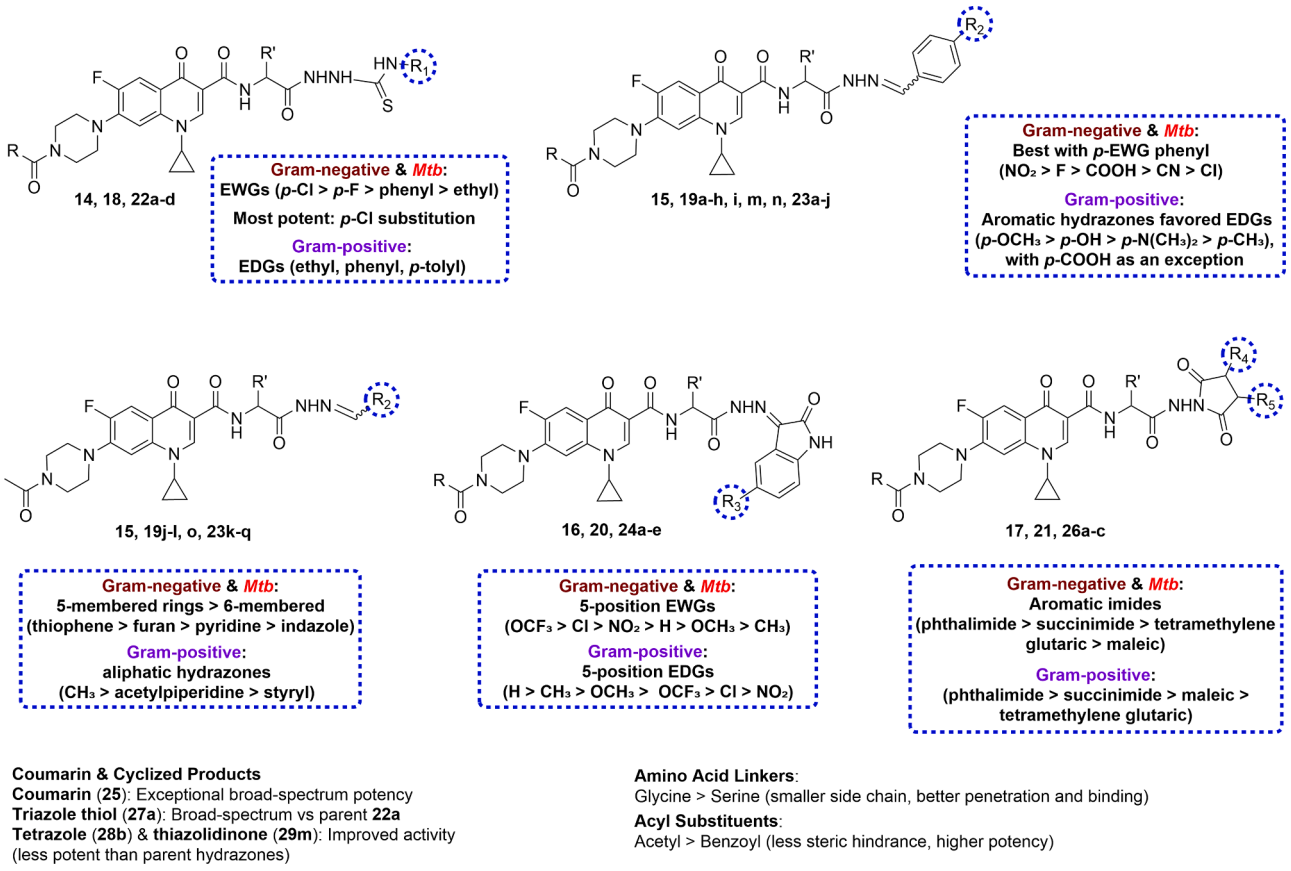

Fig. 2. Structure-activity relationship (SAR) of the ciprofloxacin conjugates.

the isatin hybrids may be related to the structural characteristics of the rigid isatin scaffold; however, further studies are required to establish the underlying mechanism. In the cyclic imide series, Gram-negative activity followed phthalimide > succinimide > tetramethylene glutaric > maleic, while for Gram-positive bacteria, activity followed phthalimide > succinimide > maleic > tetramethylene glutaric. Compound 21a exhibited reasonable activity against MRSA (MIC 15.71 μM). The coumarin derivative 25 exhibited particularly strong and broad-spectrum activity, with potency against *S. aureus* (MIC 0.47 μM), MRSA (MIC 3.41 μM), and *M. tuberculosis* (MIC 1.58 μM). Cyclization of ethylthiosemicarbazide 22a yielded 27a (a triazole thiol), which demonstrated broad-spectrum efficacy across Gram-positive and Gram-negative bacteria (Fig. 2). It exhibited MIC values of 1.38 μM against *S. aureus* and 7.36 μM against MDR *E. coli*. Tetrazole 28b and thiazolidinone 29m also improved antibacterial activity but remained less potent than their parent hydrazones. The decreased potency may be related to the structural changes introduced by cyclization; however, the precise mechanism requires further investigation.

Glycine-based derivatives were more active than serine analogs, while acetyl-substituted compounds were more potent than benzoyl analogs. Overall, electron-withdrawing substituents and heterocycles were associated with higher activity against Gram-negative bacteria and *M. tuberculosis*, whereas electron-donating groups were generally associated with higher Gram-positive activity. Hybridization with rigid scaffolds such as isatin and coumarin was associated with enhanced activity, while cyclization of hydrazones generally reduced potency (Pai and Bhat, 2026; Guo, 2019). It should be noted that some hydrazone and isatin derivatives were evaluated as *E/Z* mixtures in the biological assays, which should be considered when interpreting the observed SAR trends.

2.2.2. *Phenotypic mode-of-action studies*

To investigate the cellular effects of the new compounds and assess whether their phenotypic profiles are consistent with inhibition of DNA gyrase and topoisomerase IV, phenotypic mode-of-action studies were performed using bacterial cytological profiling (BCP) in live bacterial cells. BCP combines phase contrast microscopy with fluorescent dyes and protein fusions that report on different cellular parameters, allowing the assessment of the effects of antibiotics on several cellular structures and functions in one assay (Schäfer et al., 2024). Due to the different principal targets of FQs in Gram-negative and Gram-positive bacteria, we applied BCP to both *E. coli* and the Gram-positive model *Bacillus subtilis*. Inhibition of topoisomerase function (including both gyrase and topoisomerase IV) elicits a characteristic and highly specific phenotype that consists of clear nucleoid packing defects, typically a strongly condensed, often oval-shaped nucleoid at mid cell, but relaxed and fragmented DNA can also be observed in some cases (Kamal El-sagheir et al., 2026). Due to the orchestration of replication and cell division, FQs further disrupt cytokinesis, resulting in the disruption of Z-ring formation and cell elongation or aberrant division events (Adams et al., 2014). Together, these phenotypes give a reliable indication for topoisomerase inhibition in live bacterial cells.

In *E. coli*, nucleoid compaction and cell elongation are the dominant FQ-induced phenotypes (Kamal El-sagheir et al., 2023a; Kamal El-sagheir et al., 2026), which can be visualized by DAPI staining and phase contrast microscopy, respectively. Additional effects on the cell envelope can be observed through membrane staining with FM4–64. Fig. 3 shows BCP images of *E. coli* W3110 co-stained with both dyes, Fig. 4A shows the quantification of cell length, and Table 1 shows a summary of all BCP results. Compounds 15b, 15h, 15j, 19k, 20b, 20e, 22d, 23c, 23h, 24b, and 27a showed a highly typical gyrase inhibition phenotype with clear nucleoid compaction, corresponding anucleic areas, and significant cell elongation. Compounds 8a and 8b showed the

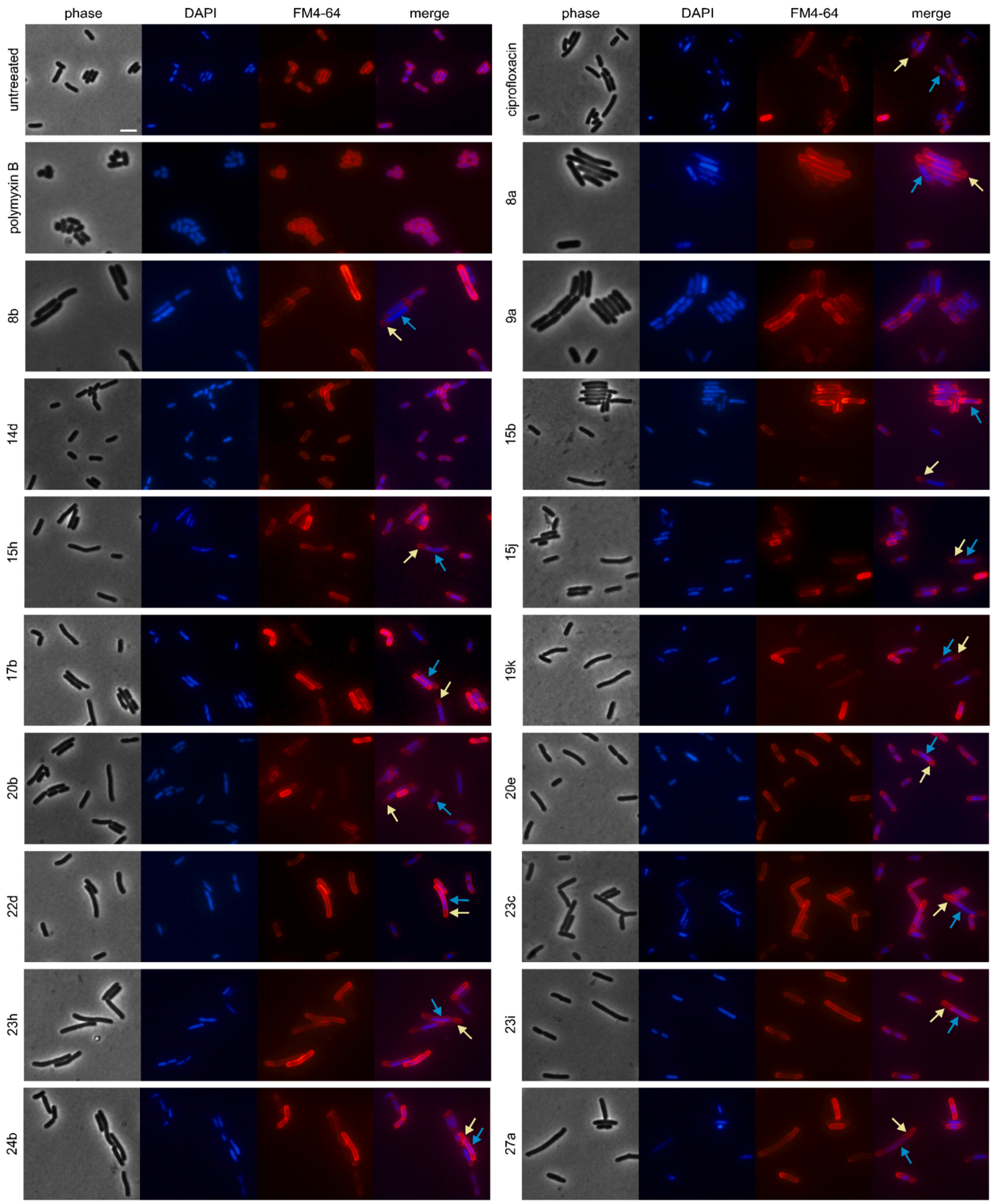

Fig. 3. Bacterial cytological profiling of *E. coli* W3110 stained with DAPI (DNA) and FM4–64 (membrane). Cultures were treated with 1 × MIC for 60 min. Blue arrows indicate condensed nucleoids and yellow arrows corresponding anucleic areas (merge panels). Representative images from three independent experiments are shown. Images were recorded and processed with identical capture settings. Scale bar: 2 μm.

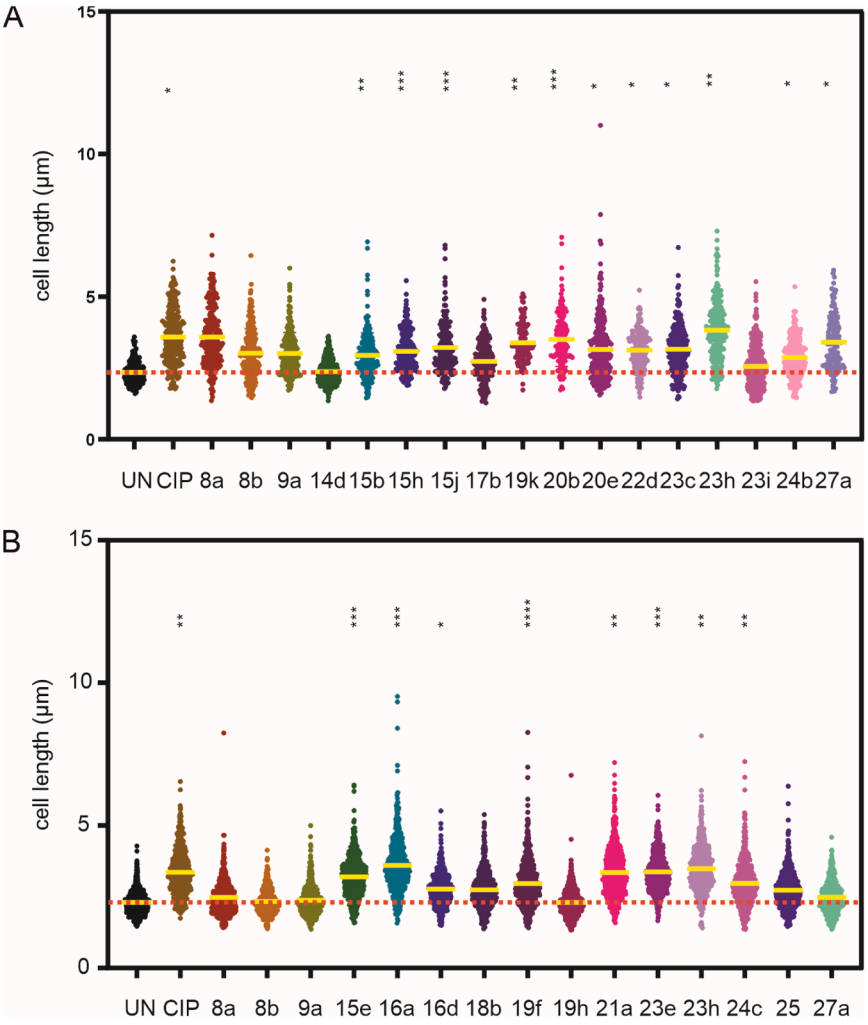

Fig. 4. Cell length measurements from BCP images of *E. coli* W3110 (A) and *B. subtilis* 2020 (B). Graphs show pooled data from three independent biological replicate experiments. Yellow bars indicate the mean cell length for each sample. The dotted red line indicates the mean of the untreated control. The total number of cells analyzed per condition ranged from 97 to 549 (Rep1), 77–339 (Rep2), and 44–242 (Rep3) for *E. coli* W3110, and from 274 to 880 (Rep1), 271–607 (Rep2), and 176–891 (Rep3) for *B. subtilis* 2020. Statistical significance was determined using two-tailed nested *t*-tests ($p < 0.05$, *$p < 0.01$, **$p < 0.001$, ***$p < 0.0001$).

Table 1
Summary of phenotypic observations made for *E. coli* W3110. UN: untreated, Cip: ciprofloxacin, PolB: polymyxin B, x: effect observed, *tendency observed but not statistically significant due to high replicate-to-replicate variation.

	shape			membrane		nucleoid			Phenotype	
	Normal	elongated	rounded	smooth	aberrant stain	regular	condensed	anucleic areas	gyrase-related effects	cell envelope
UN	x			x		x				
Cip		x		x			x	x	x	
PolB			x	x		x				x
8a	x	*		x			x	x	x	
8b	x	*		x			x	x	x	
9a	x	*		x		x				
14d	x			x		x				
15b		x		x			x	x	x	
15h		x		x			x	x	x	
15j		x		x			x	x	x	
17b	x			x			x	x	x	
19k		x		x			x	x	x	
20b		x		x			x	x	x	
20e		x		x			x	x	x	
22d		x		x			x	x	x	
23c		x		x			x	x	x	
23h		x		x			x	x	x	
23i	x			x			x	x	x	
24b		x		x			x	x	x	
27a		x		x			x	x	x	

same phenotypes, but cell length measurements, despite a clear tendency toward elongation, were not statistically significant due to high replicate-to-replicate variation. Compounds 12b and 23i showed nucleoid compaction and anucleic areas but no cell elongation, suggesting that they may affect gyrase activity but not to an extent that visibly disrupts cell division at the tested concentrations and timeframes (1 × MIC, 60 min). Compounds 9a and 14d did not show clear DNA packing defects, suggesting that they are not effective gyrase inhibitors in *E. coli* cells. No compound showed an aberrant phenotype in the FM4–64 stain or cell shape aberrations indicative of cell envelope disturbances beyond division defects (*e.g.*, reduced cell length and a rounded shape as observed for polymyxin B).

As for *E. coli*, nucleoid compaction and cell elongation are markers for topoisomerase inhibition in *B. subtilis* as well (Kamal El-sagheir et al., 2023b; Kamal El-sagheir et al., 2023c). However, relaxed and fragmented nucleoids can also be observed (Kamal El-sagheir et al., 2026; Chiriac et al., 2015). Additionally, elongation can be suppressed by additional effects on the cell envelope and energy metabolism or induced by interference with other processes including the direct impairment of cell division components, topoisomerase-independent DNA damage, and inhibition of cell wall synthesis, among others (Araújo-Bazán et al., 2016). Elongation is therefore a phenotype that, when observed in concert with nucleoid compaction, supports the diagnosis of topoisomerase inhibition, but is neither sufficient to confirm this mechanism and nor does its absence necessarily rule it out. It is therefore beneficial to, in addition to DNA and membrane staining, also observe FtsZ localization as the characteristic double and off-center ring patterns observed with FQs clearly set topoisomerase inhibition apart from other effects on the divisome, including direct interference with FtsZ polymerization and treadmilling (Araújo-Bazán et al., 2016). Together, FtsZ localization, DNA, and membrane staining provide complementary phenotypic evidence supporting topoisomerase inhibition in *B. subtilis*, although they do not individually establish direct molecular targeting.

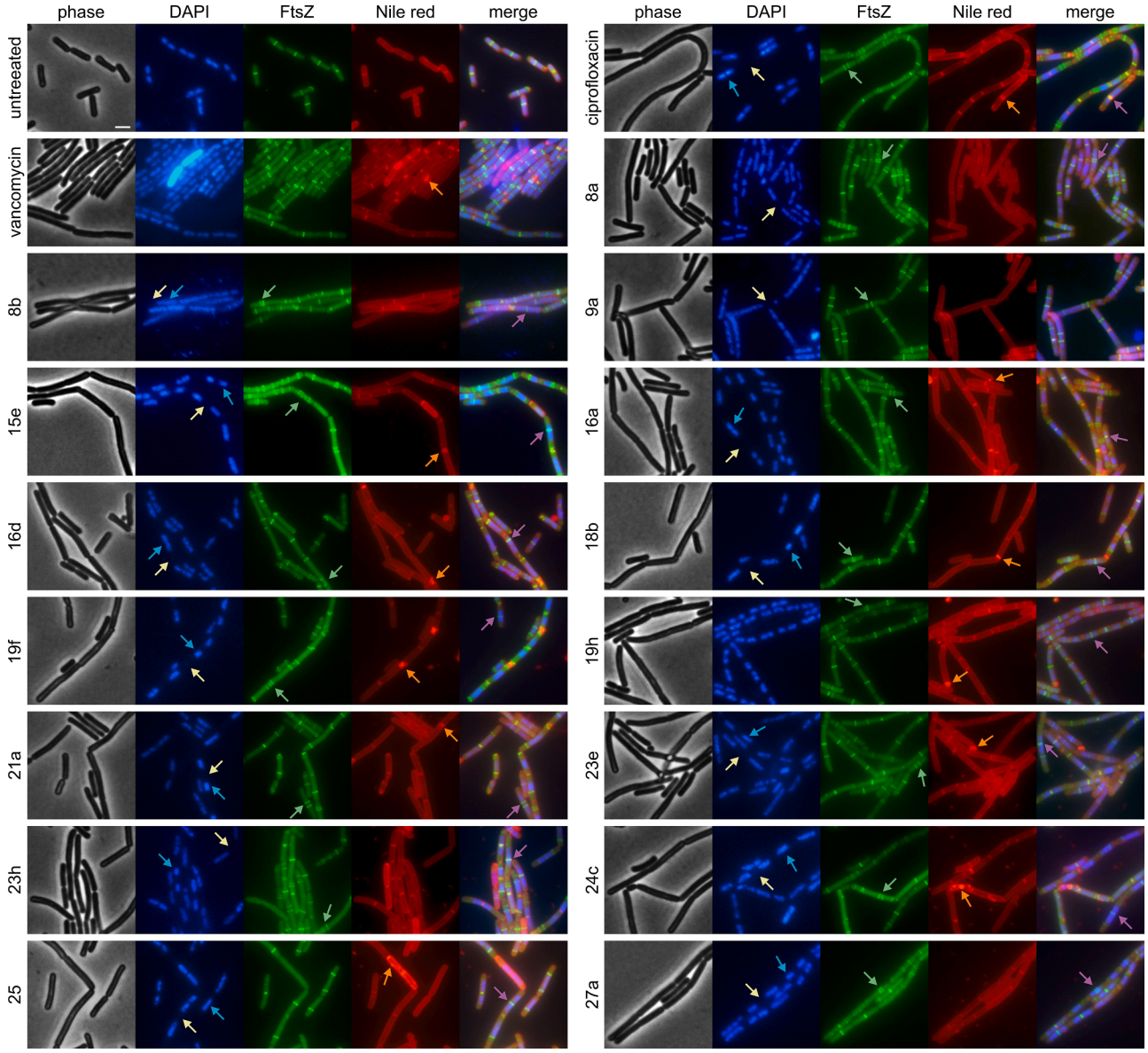

Fig. 5. Bacterial cytological profiling of *B. subtilis* 2020 (*Pxyl-ftsz-gfp*) stained with DAPI (DNA) and Nile red (membrane). Cultures were treated with 1 × MIC for 60 min with the exception of vancomycin, for which 30 min were chosen to avoid lysis phenotypes. Blue arrows indicate condensed nucleoids (DAPI panels), yellow arrows corresponding anucleic areas (DAPI panels), green arrows double or multiple Z rings (FtsZ panels), red arrows aberrant membrane stains (Nile red panels), and purple arrows Z rings formed over nucleoids (merge panels). Representative images from three independent experiments are shown. Images were recorded and processed with identical capture settings. Scale bar: 2 μm.

Fig. 5 shows BCP images of *B. subtilis* 2020 (*Pxyl-ftsZ-gfp*), expressing a green-fluorescent protein (GFP) fusion to FtsZ, stained with DAPI and the membrane dye Nile red. Fig. 4B shows the quantification of cell length and Table 2 an overview of BCP results. While most compounds showed clear nucleoid compaction and corresponding anucleic areas, 9a instead showed relaxation and fragmentation, while 8b and 16d showed both phenotypes. Yet, no complete fragmentation of the nucleoid was observed, suggesting that these phenotypes are attributable to topoisomerase inhibition instead of direct DNA-damaging activity (Özsan et al., 2026; Kamal El-sagheir et al., 2023a). Compounds 15e, 16a, 16d, 19f, 21a, 23e, 23h, and 24c showed characteristic topoisomerase phenotypes on all accounts, including nucleoid compaction, anucleic areas, statistically significant cell elongation, double and off-center Z rings, as well as Z rings forming over the nucleoid indicating a dysfunctional nucleoid occlusion (noc) system. Additionally, compounds 8b, 18b, 25, and 27a showed all characteristics of topoisomerase inhibition except significant elongation. Compounds 8a, 9a, and 19h showed mixed phenotypes. Thereby compounds 8a and 9a showed some topoisomerase inhibition characteristics in both nucleoid compaction and FtsZ localization, while 19h only showed aberrant FtsZ localization. While topoisomerase inhibition cannot be clearly confirmed for these compounds in live *B. subtilis*, 8a and 9a are more likely to inhibit topoisomerases at least as part of their mechanisms of action, while this cannot be concluded for 19h, at least at the concentrations and time frames tested here (1 × MIC, 60 min).

The Nile red stain showed aberrant foci for compounds 15e, 16a, 16d, 18b, 19f, 19h, 21a, 23e, 24c, and 25. However, membrane foci can have several causes in *B. subtilis* and are observed with both cell envelope-targeting compounds such as vancomycin and with FQs. However, no effects deviating from the ciprofloxacin membrane phenotype were observed suggesting no atypical effects on the cell envelope. This was confirmed by the clearly membrane-associated localization of FtsZ, as the protein detaches from the cell membrane upon depolarization (Strahl and Hamoen, 2010; Saeloh et al., 2017). To further explore secondary effects on the cell envelope, the localization and mobility of MreB were examined using *B. subtilis* MW10 (*Pxyl-gfp-mreB*) expressing a GFP fusion to this protein. MreB orchestrates lateral cell wall synthesis and reacts differently to membrane damage and cell wall synthesis inhibition. Upon depolarization, portions of cellular MreB accumulate in immobile clusters while the remaining MreB retains its typical helical pattern along the lateral cell periphery. Similar observations can be made with compounds disrupting membrane domain organization, while a complete collapse of the membrane potential typically leads to detachment of the protein from the cell membrane (Strahl and Hamoen, 2010; Wenzel et al., 2018; Strahl et al., 2014). None of these phenotypes were observed with any of the new derivatives, confirming the notion that they do not interfere with the cell membrane. MreB also serves as marker for cell wall synthesis inhibition as its helical movement along the lateral cell axis depends on lipid-linked cell wall precursors and stops upon inhibition of peptidoglycan or wall teichoic acid synthesis (Kamal El-sagheir et al., 2023b, 2023c; Strahl et al., 2014). To assess possible effects on cell wall synthesis, MreB mobility was assessed (Fig. 6). No derivative abolished MreB movement, excluding secondary mechanisms involving cell wall synthesis. However, cultures treated with compound 16a showed a minor but reliably reproducible subpopulation of cells with completely stalled MreB movement and large MreB foci resembling cells treated with the positive control vancomycin (4.7% ±1.5%). Note that untreated control cells did not show this phenotype at all (0%) while vancomycin-treated cultures exhibited entirely immobile cell populations (100%). This observation suggests that 16a can under certain conditions affect cell wall synthesis, possibly in already pre-stressed subpopulations. Whether or not this property may be of relevance in clinical strains and under infection conditions remains to be investigated.

Table 2
Summary of phenotypic observations made for *B. subtilis*. UN: untreated, Cip: ciprofloxacin, Van: vancomycin, x: effect observed, *observed in minor subpopulation of cells (4.7% ±1.5%). "Foci" correspond to large, single Nile red foci and "spotty" to many small Nile red spots across the cell membrane. "Smooth" denotes cells with a normal membrane stain. "Regular", "double rings", "off-center rings," and "rings over DNA" denote the corresponding aberrant FtsZ localization patterns; "mobile" and "immobile" refer to MreB mobility phenotypes.

	shape		membrane			DNA				FtsZ					MreB		Phenotype	
	normal	elongated	smooth	foci	spotty	regular	condensed	anucleic areas	relaxed	fragmented	regular	double rings	off-center rings	rings over DNA	cytosolic	mobile	immobile	topoisomerase-related effects	cell envelope
UN	x		x			x					x					x			
Cip		x		x			x	x				X	x	x		x		x	
Van	x			x		x					x						x		x
8a		x	x			x		x				X		x		x			
8b	x		x				x	x		x		X	x	x		x		x	
9a	x		x					x	x	x		X		x		x			
15e		x		x			x	x				X	x	x		x		x	
16a		x		x			x	x				X	x	x			*	x	x
16d		x		x			x	x		x		X	x	x		x		x	
18b	x			x			x	x				X	x	x		x		x	
19f		x		x			x	x				X	x	x		x		x	
19h	x			x		x						X	x	x		x			
21a		x		x			x	x				X	x	x		x		x	
23e		x		x			x	x				X	x	x		x		x	
23h		x	x				x	x				X	x	x		x		x	
24c		x		x			x	x				X	x	x		x		x	
25	x			x			x	x					x	x		x		x	
27a	x		x				x	x				X	x	x		x		x	

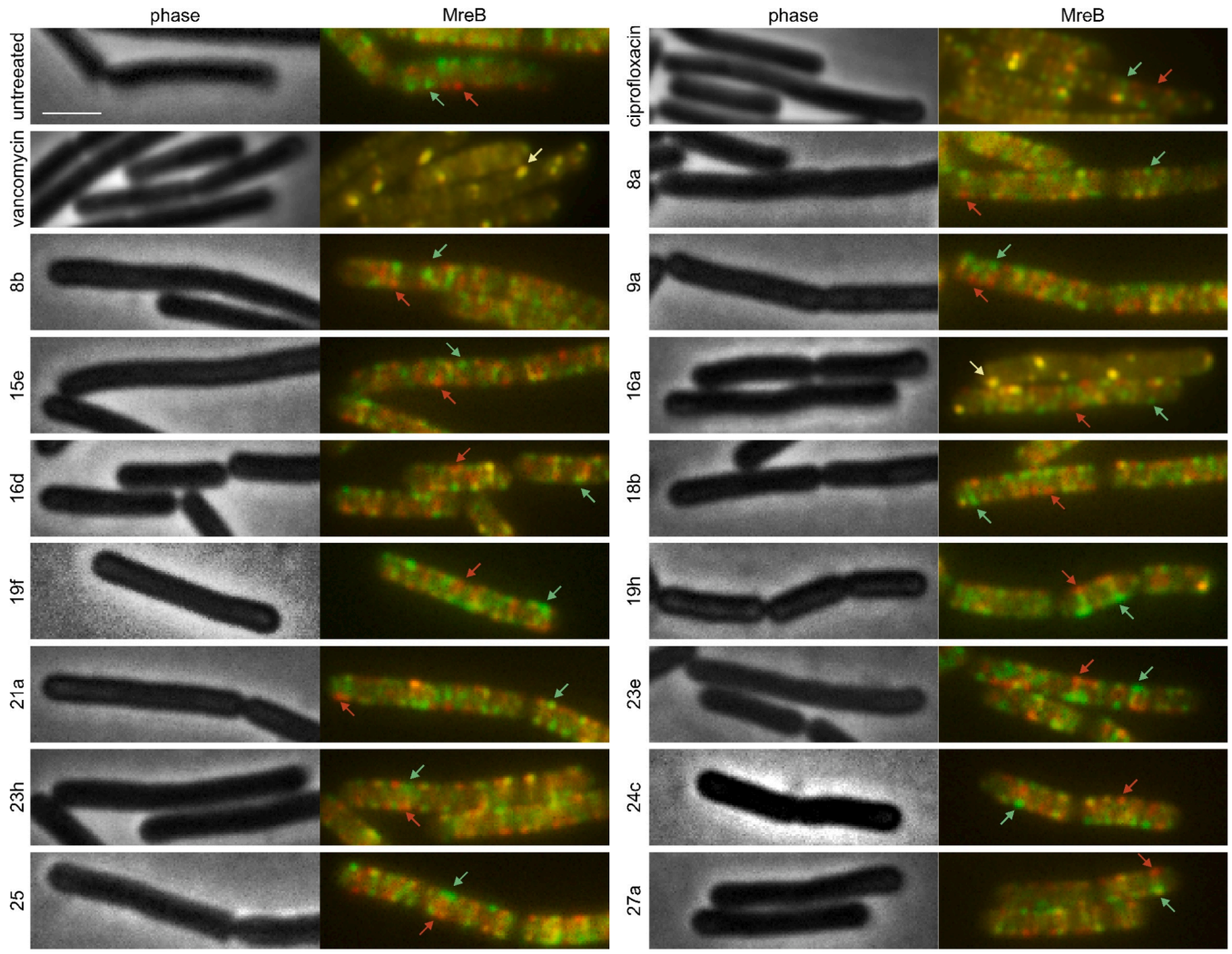

Fig. 6. MreB mobility assay using *B. subtilis* MW10 (*Pxyl-gfp-mreB*). Two separate images were taken of the same field of view in a 30-second interval. Due to MreB movement, false-colored overlays of the resulting frames will show distinct red and green foci (untreated control). In cell wall biosynthesis-impaired cells, MreB movement is abolished, resulting in exact overlays showing all-yellow MreB foci (vancomycin control). Cultures were treated with 1 × MIC for 60 min with the exception of vancomycin, for which 30 min were chosen to avoid lysis phenotypes. Green and red arrows indicate mobile MreB foci, yellow arrows immobile foci. Representative images from three independent experiments are shown. Images were recorded and processed with identical capture and display settings. Scale bar 2 μm.

2.2.3. Antibiofilm activity

To assess the effects of the new derivatives on biofilm-associated biomass, minimal biofilm-inhibitory concentrations (MBICs) were determined against *S. aureus* ATCC 6538 using a modified crystal violet assay based on the protocol of O'Toole (O'Toole, 2011). Biofilm-associated biomass was quantified by crystal violet staining at

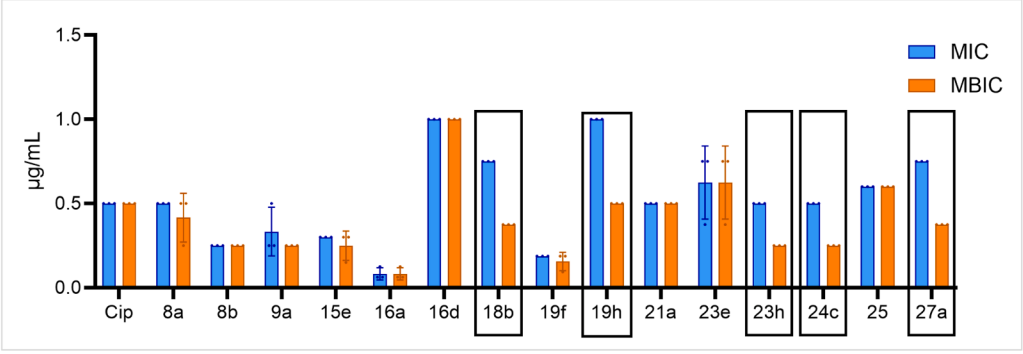

Fig. 7. Minimal biofilm-inhibiting concentrations (MBICs) compared to minimal inhibitory concentrations (MICs) determined against *S. aureus* ATCC 6538 in the same assay. Black boxes indicate compounds with reliably reproducible biofilm inhibition activity at sub-MIC. Error bars represent standard deviation of the mean. Individual datapoints from biological triplicate experiments are indicated as dots.

570 nm following compound exposure, with MICs determined under the same assay conditions. Compounds showing reproducible reductions in attached biomass at sub-MIC concentrations were considered active in the assay. This was the case for compounds 18b, 19h, 23h, 24c, and 27a (MBICs 0.25–0.5 μg/mL; 0.41–0.78 μM), which all showed reproducible biofilm inhibition at 0.5 × MIC (Fig. 7). These findings indicate that the tested compounds reduce crystal violet-stained attached biomass at sub-MIC concentrations. However, without growth-normalized measurements or an independent viability assay, these reductions may reflect decreased bacterial growth or viability and do not establish a biofilm-specific mechanism. Compared with previously reported fluoroquinolone derivatives, several compounds showed greater reductions in attached biomass at sub-MIC concentrations, warranting further investigation (El-sagheir et al., 2025a).

2.2.4. DNA gyrase and topoisomerase IV inhibition assay

We next determined IC_{50} values of the most active candidates against *E. coli* and *S. aureus* against the DNA gyrase and topoisomerase IV enzymes *in vitro* (Fig. 8 and Table S4), using the cleavage-complex stabilization method (Burrell et al., 2010). This assay relies on the enzymes' ability to relax supercoiled pBR322 DNA through transient double-strand break formation. FQs effectively stabilize the enzyme–DNA complex, forming a non-functional ternary complex (Medellín-Luna et al., 2023). The tested compounds exhibited strong inhibitory activity against DNA gyrase, with IC_{50} values ranging from 0.19 to 1.01 μM, corresponding to equal or up to 5.2-fold greater activity than ciprofloxacin. Additionally, compounds 15b, 17b, and 19k displayed 1.3- to 2.1-fold stronger activity than the parent hydrazide 8a. Collectively, compounds 14d, 15b, 17b, 19k, and 24b are the most promising DNA gyrase inhibitors. These derivatives possess pharmacophores such as *p*-chlorophenyl thiosemicarbazide, *p*-nitrophenyl hydrazone, succinimide, thiophene hydrazone, and 5-chloroisatin. Their enhanced activities indicated that incorporating electron-withdrawing groups, and heteroaromatic motifs could significantly improve the binding affinity and inhibitory potential of ciprofloxacin toward DNA gyrase. The observed DNA gyrase inhibitory activity is comparable to that reported for other modified fluoroquinolone derivatives, supporting the potential of the introduced substituents to preserve or enhance the target-directed activity of the fluoroquinolone scaffold. Regarding topoisomerase IV, the most potent compounds showed IC_{50} values ranging from 1.68 to 7.12 μM, representing a 1.7–4.2-fold improvement over ciprofloxacin. The most active inhibitors were 15e and 23e (*p*-methoxyphenyl hydrazones), 16a (isatin hybrid), 19f (*p*-hydroxyphenyl hydrazone), 25 (coumarin hybrid), and 27a (triazole thiol). The enhanced activity of these derivatives can be attributed to the presence of electron-donating groups, heterocyclic frameworks, and bioactive scaffolds such as isatin and coumarin. These structural features likely improve binding interactions and overall inhibitory potency. Importantly, the investigated compounds showed favorable selectivity toward bacterial gyrase over human topoisomerase II, with IC_{50} values ranging from 58.97 to 80.13 μM, compared with 19.41 μM for etoposide (Etoposide).

2.2.5. Urease enzyme assay

Next, urease inhibition was evaluated using the established indophenol assay (Shi et al., 2016). This method provides a sensitive and reliable measure of quantifying ammonia and is based on the formation of an indophenol blue complex generated through the Berthelot reaction involving ammonia, chlorine, and a phenolic reagent (Tzollas et al., 2010). The inhibitory activities of the synthesized compounds were determined (Fig. 9 and Table S6), and compared with acetohydroxamic acid (AHA), a recognized urease inhibitor, as well as ciprofloxacin (Cip). The investigated compounds exhibited IC_{50} values ranging from 10.1 to 37.3 μM and showed higher inhibitory activity than AHA, with a 1.3–4.9-fold improvement. Additionally, most compounds demonstrated 1.5–3.2-fold greater potency than the parent compound Cip. The most active urease inhibitors were compounds 14d (*p*-chlorophenyl thiosemicarbazide), 15j (furan hydrazone), 19c (*p*-fluorophenyl hydrazone), 20b (5-chloroisatin hybrid), 22d (*p*-fluorophenyl thiosemicarbazide), and 23h (*p*-carboxyphenyl hydrazone). The promising activity of these molecules can be attributed to enhanced binding affinity and interactions within the urease active site. This improvement is likely due to the presence of electron-withdrawing substituents and heterocyclic motifs such as furan and isatin. Additionally, these functionalities are capable of forming strong hydrogen-bond interactions and metal chelation, particularly thiosemicarbazides, which further contribute to the improved inhibitory potency.

Notably, the urease-inhibitory activity showed a consistent trend with the observed MICs against *H. pylori*, which relies on urease to survive the acidic conditions of the stomach, suggesting that urease inhibition may contribute to the observed antimicrobial activity. However, because the biochemical assay was performed using jack bean urease rather than *H. pylori* urease, this relationship should be interpreted as suggestive rather than direct evidence of inhibition of the bacterial enzyme. The observed urease-inhibitory activity was also comparable to that reported for previously described fluoroquinolone hydroxamic and hydrazide derivatives, suggesting that the structural modifications introduced in the present study may preserve urease-inhibitory activity while providing additional antibacterial effects (Abdullah et al., 2017).

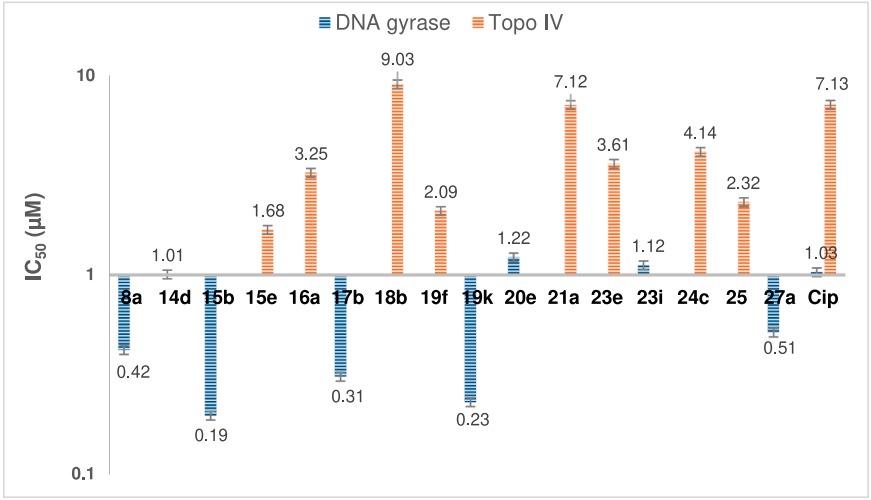

Fig. 8. IC_{50} values (μM) of the studied compounds against DNA gyrase and topoisomerase IV. IC_{50} values (means ± SD) were determined from triplicate experiments.

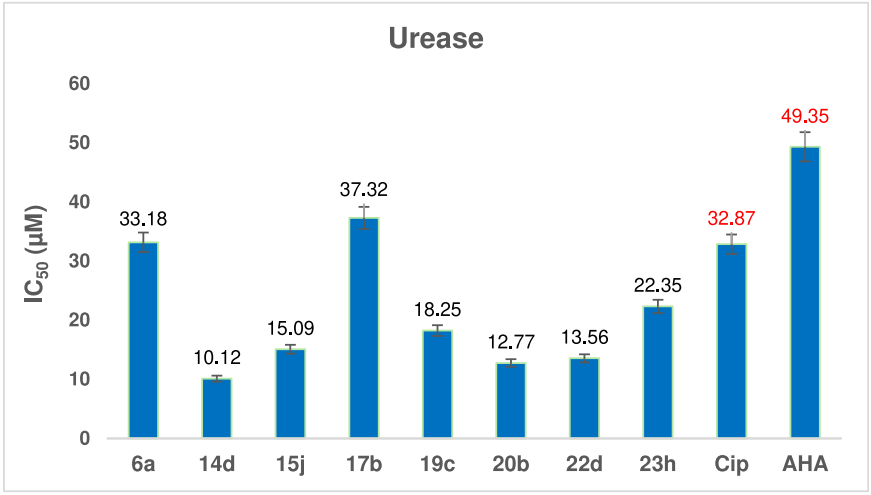

Fig. 9. IC_{50} values (μM) of the studied compounds against Jack bean urease. IC_{50} values are presented as mean ± standard deviation (SD) from three independent measurements.

2.2.6. Killing kinetics, resistance development, and cytotoxicity

To gain further insight into the promise of the new compounds, time-kill kinetics were performed for the most active derivatives 15e, 16a, 18b, 19f, 23e, 24c, and 25 to determine whether they exert bacteriostatic or bactericidal effects. The evaluation was performed against *S. aureus* ATCC 6538 by determining their minimal bactericidal concentrations (MBCs). The compounds showed MBC values of 0.9–4.34 μM, markedly lower than Cip (MBC 8.30 μM) (Table S7). Their MBC/MIC ratios of *ca.* 1–3 further confirm that they act as bactericidal agents under the tested conditions (Gonzalez et al., 2013).

The bactericidal activity of the newly designed compound 15e (as a representative example) was further evaluated *in vitro* using a time-kill assay at 1 ×, 2 ×, 4 ×, and 8 × MIC, with Cip as a positive control (Fig. 10). At 1 × MIC, both 15e and Cip were bacteriostatic. Increasing the concentration of 15e resulted in progressively faster bactericidal activity, with killing observed earlier than with Cip at both 2 × and 4 × MIC. At 8 × MIC, 15e produced a > 3-log CFU reduction within 2 h and complete eradication by 4 h, whereas Cip showed no additional killing effect. After 24 h, 15e reduced bacterial counts by ≥6 logs. These findings demonstrate that the lead compound 15e exhibits faster bactericidal kinetics than Cip while retaining the ability of FQs to induce bacterial cell death.

Next, we evaluated the potential for bacterial resistance development to our new antimicrobial agents. Compound 25 was tested against *S. aureus* and 15b against *E. coli*, with Cip as a reference drug. Bacteria were repeatedly exposed to sub-MIC concentrations of each compound over 20 days, and resistance was defined as a > 4-fold increase in MIC (reference line). As shown in Fig. 11, the MICs of 25 and 15b remained largely stable throughout the study, exhibiting only minor 2–3-fold increases. In contrast, Cip's MIC increased dramatically, by *ca.* 48-fold for *S. aureus* and *ca.* 32-fold for *E. coli*. These findings provide primary evidence that the selected compounds, 25 and 15b, have a lower propensity for resistance emergence than Cip under the tested conditions, supporting their potential as antimicrobial candidates. However, these findings are limited to the two selected compounds and bacterial strains and should not be generalized to the entire chemical series.

Finally, we examined the cytotoxicity of representative compounds from each series, chosen according to their potency profiles. An MTT cell viability assay was performed using human neuroblastoma (SH-SY5Y) and normal diploid fibroblast (WI-38) cell lines (Li et al., 2016; Dam et al., 2017). Ciprofloxacin and the apoptosis-inducing kinase inhibitor staurosporine were employed as reference compounds. All tested

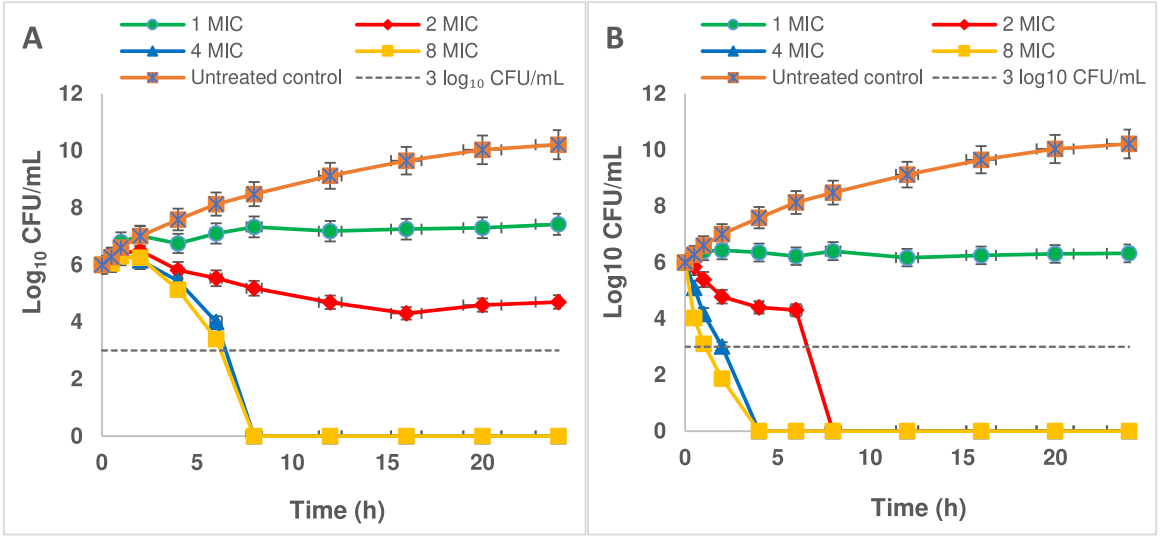

Fig. 10. Time-kill curves showing the bactericidal activity of (A) ciprofloxacin (Cip) and (B) 15e against *S. aureus*. Values shown as zero indicate that no colonies were detected. Data are presented as mean values from three independent experiments.

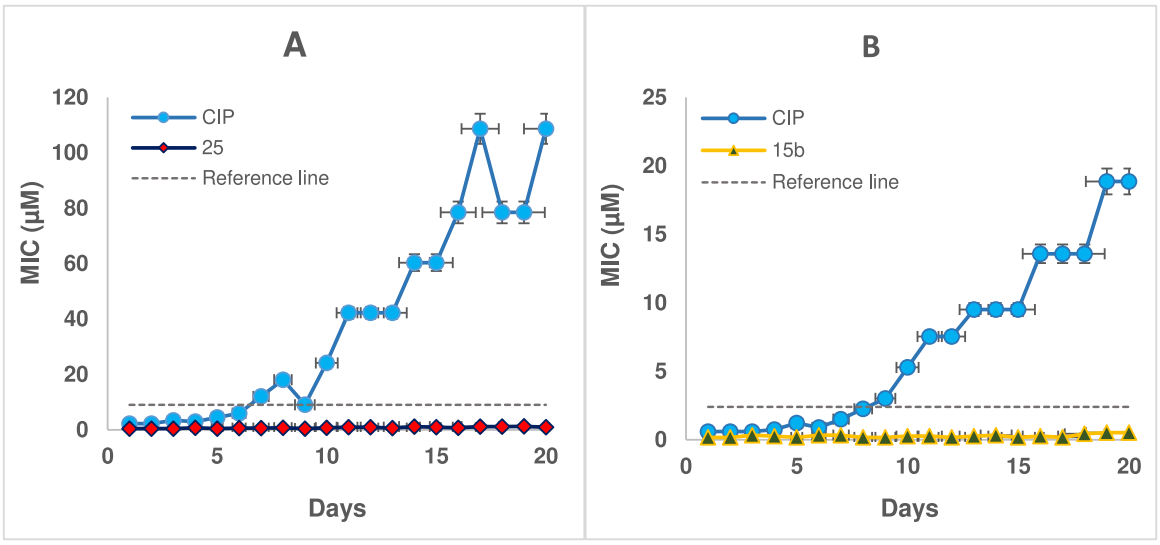

Fig. 11. Development of bacterial resistance to the tested compounds and ciprofloxacin (Cip); (A) *S. aureus*; (B) *E. coli*.

compounds showed low cytotoxicity (IC_{50} >50 μM) toward both cell lines (Table 3). The IC_{50} values were higher than that of staurosporine (about 3.3-fold on SH-SY5Y and 4.7-fold on WI-38), and their cytotoxic profiles were broadly comparable to ciprofloxacin. The new derivatives demonstrated IC_{50} values of 50.23–66.5 μM against SH-SY5Y cells and 61.78–81.14 μM against WI-38 cells. These findings indicate low cytotoxic effects on the two tested mammalian cell lines under the experimental conditions and provide primary evidence supporting the safety and cellular selectivity of the tested compounds. While these results do not establish an overall safety profile or directly assess neurotoxicity, the absence of significant cytotoxicity in SH-SY5Y cells provides preliminary evidence of low cytotoxic effects in this neuronal cell model.

Based on these results, we further assessed the bacterial selectivity of the compounds relative to ciprofloxacin. The selectivity index (SI) was calculated as the ratio of cytotoxicity IC_{50} to MIC, using WI-38 IC_{50} values and resistant *E. coli* and MRSA MIC values. The tested compounds exhibited SI values of 10–23 (SI >10), indicating a difference between the concentrations associated with cytotoxicity in WI-38 cells and those required for antibacterial activity under the tested conditions (Cheerala et al., 2023). Notably, the calculated SI values were comparable to or higher than that of the hydrazide intermediate 8a (SI = 10). Taken together, these results provide preliminary evidence of bacterial selectivity and low cytotoxicity in the tested cell lines, while further studies using additional cell models and experimental systems are required to assess broader safety and off-target effects.

Table 3
IC_{50} (μM) of selected compounds on SH-SY5Y and WI-38. IC_{50} values, expressed as mean ± SD, were obtained from three independent experiments.

Compound		Cytotoxicity IC_{50} (μM)		SI*	
Code	MW	SH-SY5Y	WI-38	*E. coli*	MRSA
8a	444.47	52.44±2.62	63.76±3.21	10	——
14d	614.17	53.31±2.89	68.56±3.23	11	——
15b	577.57	57.43±2.55	70.88±3.71	16	——
16a	573.58	50.23 ± 2.08	61.78±2.92	——	12
19f	601.66	66.50±3.24	81.14±4.47	——	20
19k	600.67	64.27±3.62	76.32±3.19	12	——
23i	638.05	54.65±2.73	64.44±3.39	15	——
25	630.63	60.71±3.11	78.16±4.05	——	23
Cip	331.3	60.02±2.97	71.26±3.48	——	——
Staurosporine	466.54	17.74±0.85	15.09±0.63	——	——

SI* (selectivity index): IC_{50}(WI-38)/MIC, calculated separately using the MIC against resistant *E. coli* and MRSA. Good selectivity: SI > 10.

2.3. Molecular modeling studies

2.3.1. Molecular docking and dynamics simulations

Molecular docking of the designed compounds was performed to investigate their predicted binding modes and interactions with DNA gyrase, topoisomerase IV, and urease using the established docking tools MOE, AutoDock 4.2.6, and K_{DEEP} (El-sagheir et al., 2025b; Lionta et al., 2014). For compounds capable of *E/Z* isomerism, both isomers were subjected to docking, and no significant differences were observed in their binding poses or key interactions within the target active sites. Following this, we calculated inhibition constant (*Ki*) values from binding scores to further assess their inhibitory potential.

All docked compounds interacted with key amino acid residues and metal ions at the active sites. The main interactions were hydrogen bonds, coordination bonds, π–π stacking, and π–cation, allowing favorable binding poses (Fig. 12). Most compounds exhibited binding scores exceeding −8 kcal/mol and lower than those of ciprofloxacin and moxifloxacin. Notably, compounds 15b, 17b, and 19k showed strong affinity toward DNA gyrase (−12.20, −11.88, and −12.09 kcal/mol). Compounds 15e, 19f, and 25 displayed high binding to topoisomerase IV (−12.71, −12.27, and −12.21 kcal/mol). Moreover, compounds 14d, 20b, and 22d demonstrated favorable interactions with urease (−9.66, −9.54, and −9.48 kcal/mol). For Fig. 12, representative compounds were selected from each chemical series based on their experimental evaluation against the corresponding enzymes and their relatively strong docking affinities, providing a direct illustration of the predicted binding modes in relation to the experimental findings. The docking results were generally consistent with the observed MIC and IC_{50} values, supporting the contribution of structural modifications to the binding interactions and biological activity.

To evaluate the selectivity of the designed compounds toward bacterial topoisomerases over their human counterpart, molecular docking was performed for the most active compounds (15b, 16a, 18b, 19k, 23i and 27a) against human topoisomerase II (PDB ID: 5GWK). The compounds exhibited weak binding affinities, with scores ranging from −2.71 to −5.09 kcal/mol, compared with etoposide (−7.83 kcal/mol). These results reveal a low predicted binding propensity toward the human enzyme and are consistent with the experimental findings, which showed weak inhibitory activity against human topoisomerase II. The agreement across different docking platforms reinforces the reliability of the predicted affinities. The results positioned the designed derivatives as promising broad-spectrum agents against bacterial enzymes (see Supporting Information for detailed docking results, Table S8–10,

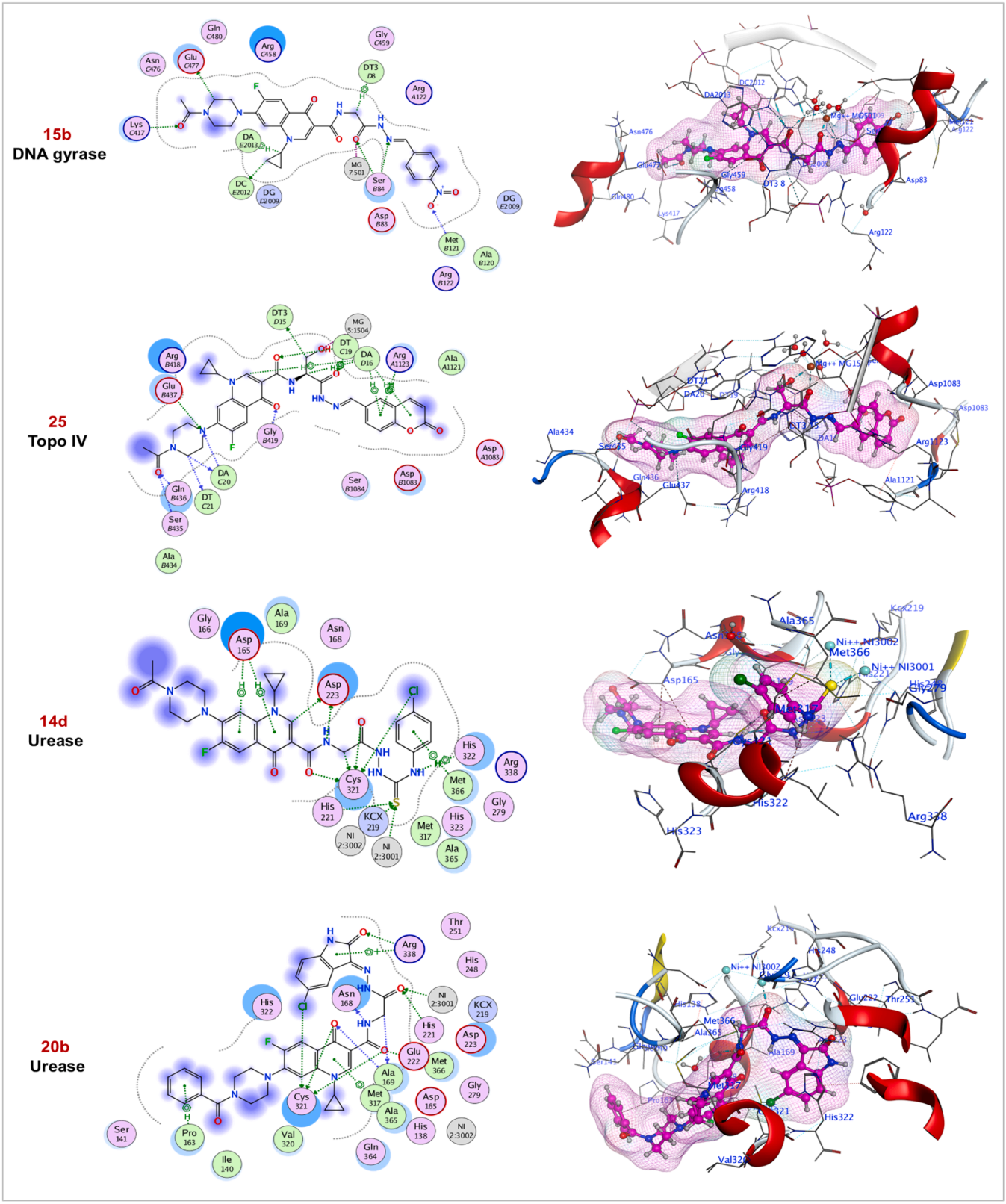

Fig. 12. 2D and 3D representation of the interactions of compounds 14d, 15b, 20b and 25 within DNA gyrase, topoisomerase IV, and urease. Compounds were selected as representative examples based on their experimental activity and relatively strong docking affinities. H-bonds and metal-ion coordination bonds are depicted in cyan, H-π bonds in red, and van der Waals clashes in orange. The ligand is represented using a ball-and-stick model, with atoms color-coded as follows: magenta for carbon, blue for nitrogen, red for oxygen, yellow for sulfur, green for fluorine, dark green for chlorine and white for hydrogen.

Fig. S208–237). The docking findings were supported by preliminary experimental metal-chelation studies performed using UV–Vis spectrophotometry with Ni^{2+}, the catalytic ion in urease. Other biologically relevant metals Zn^{2+} and Cd^{2+}, were included to evaluate the metal-binding capacity of the compounds. The designed compounds exhibited reasonable metal-binding capability, as suggested by characteristic hypochromic and bathochromic shifts in the UV–Vis spectra (Table S11 and Fig. S238).

Since DNA gyrase and topoisomerase IV are established targets of ciprofloxacin while urease is a new potential target enzyme, two independent 100 ns molecular dynamics simulations were conducted to validate the binding stability and affinity of the most active urease inhibitors (14d, 20b, and 22d). For the MD simulations, the thermodynamically most stable isomer of each compound was selected; docking of both *E/Z* isomers showed no significant differences in their binding poses or key interactions. The docked complexes with urease (PDB ID: 1e9y) were used, along with acetohydroxamic acid (AHA) as a reference (da Silva et al., 2023; Ndarawit W et al., 2024). All compounds remained stably within the active site, displaying RMSD values comparable to AHA. They also maintained key interactions with catalytic residues throughout the simulations. MM-PBSA binding free energy calculations were used to further assess the predicted binding affinities. The reported ΔG values represent the average values obtained from the two independent simulations, with more favorable values observed for compounds 14d (−10.21 kcal/mol), 20b (−10.14 kcal/mol), and 22d (−9.95 kcal/mol) compared with AHA (−7.93 kcal/mol). Both replicate simulations showed comparable RMSD profiles and reached similar equilibrium states, with only minor differences in the average RMSD values between the two runs (approximately 0.1–0.4 Å). These findings were additionally supported by consistent hydrogen bonding, enhanced ligand–protein contacts, and stable protein conformations. Overall, the MD results were consistent with the docking and biological data and provide further computational support for the potential urease-inhibitory activity of these compounds (Fig. S239–246, Table S12).

2.3.2. Quantum chemical calculations

The density functional theory (DFT) method was utilized to perform quantum chemical calculations at the B3LYP/6–311G(d,p) level. This approach provides a deeper understanding of the molecular geometry, electronic structure, and chemical reactivity of the synthesized derivatives. Molecular electrostatic potential (MEP) maps indicated that oxygen and sulfur atoms are the most electron-rich (nucleophilic) regions. In contrast, the highest positive charges are localized on nitrogen atoms and the hydrogen atoms attached to them (electrophilic regions). These regions were recognized as potential sites for interaction with biological targets. Frontier molecular orbital (FMO) analysis revealed moderate HOMO–LUMO energy gaps (5.59–7.41 eV), indicating favorable charge transfer and chemical reactivity. Calculated global reactivity descriptors (η, S, χ, μ, and ω) further suggested that the designed derivatives exhibited high softness and electrophilicity, and strong electron-accepting ability. Overall, these computational insights are consistent with experimental and docking results. They provide additional insight into the electronic characteristics and charge distribution of the new ciprofloxacin derivatives, which may be relevant to their observed antibacterial activity. Full computational methods, parameters, and detailed results are available in the Supporting Information (Figure S247–250, Table S13).

2.3.3. Quantitative structure-activity relationship (QSAR) study

QSAR models were constructed to correlate the antibacterial activity of the new derivatives with calculated molecular descriptors. A set of 69 newly synthesized derivatives was selected for the training set using a diversity-based approach rather than a simple random split, with the aim of ensuring broad and representative coverage of both chemical structural diversity and biological activity. The selection considered the major chemical series, including thiosemicarbazides, hydrazones, isatin Schiff bases, and cyclic imides, as well as antibacterial activity expressed as pMIC ($-\log_{10}$ MIC, with MIC in μM) for each bacterial species. The training and test sets were designed to represent the chemical and biological activity spaces of the investigated compounds (Table S14–15). Regarding *E/Z* isomerism, hydrazones were computationally represented by their favored predominant *E* isomers, whereas isatin Schiff bases were represented by their favored *Z* isomers. Although potential *E/Z* isomeric heterogeneity under the antibacterial assay conditions cannot be entirely excluded, the selected structures provide an experimentally supported basis for QSAR model development. 2D and 3D descriptors capturing electronic, hydrophobic, geometric, topological, and quantum mechanical properties were considered and computed. Partial least squares (PLS) regression was applied, with up to six descriptors per model to avoid overfitting and multicollinearity.

The best-performing model for *E. coli* (Equation 1) was:

$$pMIC = 1.42131 + 0.00391 * E_vdw - 0.06866 * KierFlex + 0.00276 * E_ele - 0.00108 * vol + 0.10054 * logP(o/w) + 0.00217 * TPSA$$

($n = 69$, $RMSE = 0.10438$, $R = 0.95260$, $R^2 = 0.90745$, $Q^2 = 0.75461$).

For *S. aureus* (Equation 2):

$$pMIC = 0.47902 + 0.00486 * E_vdw - 0.02931 * KierFlex + 0.05825 * Q_PC^{+} - 0.00102 * vol + 0.11017 * logP(o/w) - 0.00334 * TPSA$$

($n = 69$, $RMSE = 0.09319$, $R = 0.95977$, $R^2 = 0.92116$, $Q^2 = 0.78204$).

The QSAR models revealed that van der Waals interactions (E_vdw) and electrostatic contributions (E_ele for *E. coli*, Q_PC⁺ for *S. aureus*) positively influence activity. Moderate lipophilicity (logP) improves membrane penetration, whereas molecular flexibility (KierFlex) and volume (vol) negatively correlate with activity. Polarity (TPSA) showed species-specific effects: modest positive correlation in *E. coli* and negative correlation in *S. aureus*. External validation with 21 additional compounds gave $R^2 = 0.7389$ for *E. coli* and $R^2 = 0.7703$ for *S. aureus*, indicating model robustness and predictive ability (Table S15, Fig. S251) (Nguyen et al., 2021; Li et al., 2025). Y-randomization analysis supported the robustness of both QSAR models, yielding (cR_p^2) values of 0.7172 for *E. coli* and 0.7503 for *S. aureus*, with substantially lower average (R^2) and (Q^2) values for the randomized models than for the original models. Leverage-based applicability-domain analysis further confirmed that all training and test compounds were below the warning leverage threshold ($h^* = 0.3043$); Table S15). Overall, the QSAR models indicated that the most active derivatives tend to be moderately lipophilic, relatively rigid, and of moderate size, with van der Waals and electrostatic contributions associated with activity. These findings provide supportive insights for further structural optimization. The QSAR analysis was broadly consistent with the SAR trends and docking results.

2.3.4. Prediction of physiochemical properties (drug-likeness) and ADME/Tox profiles

The physicochemical parameters of the synthesized compounds were computed and compared to ciprofloxacin. Key descriptors involved molecular weight, logP, logS, TPSA, rotatable bond count, hydrogen-bond donors/acceptors, and ring numbers (Kaur et al., 2020). The obtained results were assessed in relation to Lipinski's, Veber's, Egan's, and Muegge's guidelines (Table S16). Most compounds exhibited favorable TPSA (81.16–148.3 $Å^2$), logP (−0.324 to 4.42), rotatable bond (4–13), and ring (4–7) values. These values were generally consistent with the criteria of the applied rules and suggested the potential for favorable oral absorption and bioavailability. Although some compounds showed deviations from Lipinski's and Veber's rules, their compliance with other complementary criteria may still support their potential drug-like properties, as discussed in the Supporting Information. The compounds showed predicted LogS values ranging from −3.04 to −5.09. Aqueous solubility was experimentally determined using

shake-flask method for representative lead compounds 15b, 19k, and 24c by UV–Vis spectroscopy and demonstrated good correlation with the computed LogS values (Fig. S252–254, Table S17). The experimental results showed agreement with the computed LogS values for these compounds; however, testing of only three lead compounds does not establish a robust correlation across the whole series.

The pharmacokinetic and toxicological properties of the new derivatives were predicted using the freely accessible pkCSM pharmacokinetics (http://structure.bioc.cam.ac.uk/pkcsm) and Pred-hERG web tool (https://predherg.labmol.com.br/). *In silico* ADME analysis revealed that the newly synthesized derivatives were predicted to have generally favorable pharmacokinetic profiles, including good intestinal absorption, appropriate distribution characteristics, and low predicted toxicity. Moreover, hERG predictions suggested a low predicted risk of QT-interval prolongation, comparable to ciprofloxacin, a marketed oral drug (Table S18). These results should be considered computational predictions rather than direct evidence of pharmacokinetic behavior or toxicological safety. Further experimental studies are required to validate these predicted properties (Raies and Bajic, 2016).

3. Conclusion

The newly synthesized hybrid derivatives demonstrated promising antimicrobial activity, with enhanced potency compared to ciprofloxacin. Some compounds showed broad-spectrum activity against different bacterial strains. This improvement was achieved through molecular hybridization of ciprofloxacin with various bioactive scaffolds such as isatin, coumarin, and other heterocycles. Among the investigated compounds, 14d, 15b, 16a, and 23h showed particularly promising activity in selected assays and may be considered representative lead candidates for further investigation. Phenotypic and anti-biofilm assays exhibited cellular phenotypes affecting cell division and inhibition of biofilm formation. The derivatives exhibited minimum bactericidal concentrations (MBCs) against *S. aureus* ranging from 0.9 to 4.34 μM, with several compounds showing greater bactericidal activity than ciprofloxacin. Furthermore, they showed faster bactericidal kinetics and a lower propensity for resistance development under the tested conditions. Regarding safety and selectivity, the compounds showed favorable selectivity indices of 10–23, indicating preferential activity toward bacterial over human cells. Molecular modeling studies highlighted favorable predicted binding affinities toward the investigated target enzymes, consistent with the observed biological activity. *In silico* evaluation of drug-likeness and ADME/Tox profiles suggested favorable oral absorption and lower potential toxicity. As a result, these hybrid surrogates emerge as promising lead compounds for further *in vivo* evaluation toward antimicrobial drug development.

4. Experimental

A series of ciprofloxacin-derived compounds was synthesized through a molecular hybridization strategy involving *N*-acylation of ciprofloxacin, coupling with amino acid esters, conversion to hydrazides, and subsequent functionalization with selected scaffolds. The synthesized compounds were purified and characterized using different analytical techniques. Their biological properties were evaluated through a panel of *in vitro* assays, including antimicrobial and antimycobacterial susceptibility testing, bacterial cytological profiling, MreB mobility, antibiofilm activity, DNA gyrase/topoisomerase IV inhibition, urease inhibition, and cytotoxicity studies. In parallel, molecular modeling studies were performed to investigate the molecular basis of activity using molecular docking, molecular dynamics simulations, quantum chemical calculations, and QSAR analysis. Detailed experimental procedures, assay conditions, characterization data, computational parameters, and additional results are provided in the Supporting Information.

CRediT authorship contribution statement

Ahmed M.Kamal El-sagheir: Writing – original draft, Visualization, Validation, Methodology, Investigation, Funding acquisition, Formal analysis, Data curation, Conceptualization. **Margareth Sidarta:** Visualization, Validation, Methodology, Investigation, Formal analysis, Data curation. **Alex Bunker:** Writing – review & editing, Validation, Supervision, Resources, Methodology, Formal analysis, Data curation. **Michaela Wenzel:** Writing – review & editing, Writing – original draft, Visualization, Validation, Supervision, Resources, Project administration, Methodology, Investigation, Funding acquisition, Formal analysis, Data curation. **Jari Yli-Kauhaluoma:** Writing – review & editing, Supervision, Resources, Project administration, Methodology, Funding acquisition, Data curation, Conceptualization.

Declaration of competing interest

The authors have declared no conflict of interest.

Acknowledgements

AE gratefully acknowledges the financial support provided by the Ministry of Higher Education of the Arab Republic of Egypt through a Ph.D. scholarship, as well as the support from the Doctoral Program in Drug Research at the University of Helsinki. MW received funding from Chalmers University of Technology. We further acknowledge CSC–IT Center for Science, Finland, for providing the computational resources essential for the molecular dynamics simulations. MW thanks Martin Andersson, Chalmers University of Technology, for access to BSL-II facilities.

Supplementary materials

Supplementary material associated with this article can be found, in the online version, at doi:10.1016/j.ejps.2026.107704.

Data availability

The authors confirm that the data supporting the findings of the study are available within the article.

References

Abd El-wahab, H.A.A., et al., 2022. New cell cycle checkpoint pathways regulators with 2-oxo-indoline scaffold as potential anticancer agents: design, synthesis, biological activities and in silico studies. Bioorg. Chem. 120, 105622.
Abdelgawad, M.A., et al., 2022. Design, synthesis, molecular modeling, and anticancer evaluation of new VEGFR-2 inhibitors based on the indolin-2-one scaffold. Pharmaceuticals 15 (11), 1416.
Abdullah, M.A., et al., 2017. Design, synthesis, molecular docking, anti-Proteus mirabilis and urease inhibition of new fluoroquinolone carboxylic acid derivatives. Bioorg. Chem. 70, 1–11.
Adams, D.W., et al., 2014. Cell cycle regulation by the bacterial nucleoid. Curr. Opin. Microbiol. 22, 94–101.
Araújo-Bazán, L., et al., 2016. Cytological profile of antibacterial FtsZ inhibitors and synthetic peptide MciZ. Front. Microbiol. 7, 1558.
Bisacchi, G.S., 2015. Origins of the quinolone class of antibacterials: an expanded "discovery story". J. Med. Chem. 58 (12), 4874–4882.
Burrell, M.R., et al., 2010. A high-throughput assay for DNA topoisomerases and other enzymes, based on DNA triplex formation. Methods Mol. Biol. 613, 257–266.
Cheerala, V.S.K., et al., 2023. Discovery of benzoxazole-thiazolidinone hybrids as promising antibacterial agents against Staphylococcus aureus and Enterococcus species. RSC Med. Chem. 14 (9), 1712–1721.
Chiriac, A.I., et al., 2015. Mode of action of closthioamide: the first member of the polythioamide class of bacterial DNA gyrase inhibitors. J. Antimicrob. Chemother. 70 (9), 2576–2588.
Clinical and Laboratory Standards Institute, 2013. Performance Standards for Antimicrobial Susceptibility Testing, 35th ed. M100-Ed35Wayne, PA, USA.
Correia, S., et al., 2017. Mechanisms of quinolone action and resistance: where do we stand? J. Med. Microbiol. 66 (5), 551–559.
da Silva, D.F., et al., 2023. Antiplasmodial activity of coumarins isolated from Polygala boliviensis: in vitro and in silico studies. J. Biomol. Struct. Dyn. 41 (22), 13383–13403.

Dam, K., et al., 2017. Increased homocysteine levels impair reference memory and reduce cortical levels of acetylcholine in a mouse model of vascular cognitive impairment. Behav. Brain Res. 321, 201–208.
Drlica, K., Zhao, X., 2021. Bacterial death from treatment with fluoroquinolones and other lethal stressors. Expert Rev. Anti-infect. Ther. 19 (5), 601–618.
El-sagheir, A.M.K., et al., 2025a. Fluoroquinolones as versatile scaffolds: potential for targeting classical and novel mechanisms to combat antibacterial resistance. Eur. J. Pharm. Sci. 214, 107247.
El-sagheir, A.M.K., et al., 2025b. Targeting OGG1 for pulmonary fibrosis: an integrated in silico study with quantum chemical calculations, docking, pharmacophore modeling, molecular dynamics, and ADMET evaluation. ChemistrySelect 10 (40), e03968.
Fàbrega, A., et al., 2009. Mechanism of action of and resistance to quinolones. Microb. Biotechnol. 2 (1), 40–61.
Fedorowicz, J., et al., 2023. Antibacterial and antibiofilm activity of permanently ionized quaternary ammonium fluoroquinolones. Eur. J. Med. Chem. 254, 115373.
Fernández-Palacios, S., et al., 2023. New insights into acylhydrazones E/Z isomerization: an experimental and theoretical approach. Int. J. Mol. Sci. 24 (19), 14739.
Fong, J., et al., 2019. Itaconimides as novel quorum sensing inhibitors of Pseudomonas aeruginosa. Front. Cell Infect. Microbiol. 8, 443.
Gonzalez, N., et al., 2013. Influence of the MBC/MIC ratio on the antibacterial activity of vancomycin versus linezolid against methicillin-resistant Staphylococcus aureus isolates in a pharmacodynamic model simulating serum and soft tissue interstitial fluid concentrations reported in diabetic patients. J. Antimicrob. Chemother. 68 (10), 2291–2295.
Guo, H., 2019. Isatin derivatives and their antibacterial activities. Eur. J. Med. Chem. 164, 678–688.
Ji, C., et al., 2015. Syntheses and antibacterial activity of N-acylated ciprofloxacin derivatives based on the trimethyl lock. ACS Med. Chem. Lett. 6 (6), 707–710.
Kadeřábková, N., et al., 2024. Antibiotic susceptibility testing using minimum inhibitory concentration (MIC) assays. NPJ Antimicrob. Resist. 2 (1), 37.
Kamal El-sagheir, A.M., et al., 2023a. Design, synthesis, molecular modeling, biological activity, and mechanism of action of novel amino acid derivatives of norfloxacin. ACS Omega 8 (45), 43271–43284.
Kamal El-sagheir, A.M., et al., 2023b. N4-substituted piperazinyl norfloxacin derivatives with broad-spectrum activity and multiple mechanisms on gyrase, topoisomerase IV, and bacterial cell wall synthesis. ACS Bio. Med. Chem. Au 3 (6), 494–506.
Kamal El-sagheir, A.M., et al., 2023c. Rational design, synthesis, molecular modeling, biological activity, and mechanism of action of polypharmacological norfloxacin hydroxamic acid derivatives. RSC Med. Chem. 14 (12), 2593–2610.
Kamal El-sagheir, A.M., et al., 2026. Design, synthesis, and integrated biological and molecular modeling studies of ciprofloxacin–amino acid derivatives as multi-target antimicrobials. Eur. J. Med. Chem. 318, 119138.
Kaur, G., et al., 2020. Theoretical molecular predictions and antimicrobial activities of newly synthesized molecular hybrids of norfloxacin and ciprofloxacin. J. Heterocyclic Chem. 57 (1), 225–237.
Li, J., et al., 2025. A review of quantitative structure-activity relationship: the development and current status of data sets, molecular descriptors and mathematical models. Chemom. Intell. Lab. Syst. 256, 105278.
Li, X., et al., 2016. Development of multifunctional pyrimidinylthiourea derivatives as potential anti-alzheimer agents. J. Med. Chem. 59 (18), 8326–8344.
Lionta, E., et al., 2014. Structure-based virtual screening for drug discovery: principles, applications and recent advances. Curr. Top. Med. Chem. 14 (16), 1923–1938.
Marc, G., et al., 2019. Design, synthesis and biological evaluation of new piperazin-4-yl-(acetyl-thiazolidine-2,4-dione) norfloxacin analogues as antimicrobial agents. Molecules 24 (21), 3959.
Medellín-Luna, M.F., et al., 2023. Fluoroquinolone analogs, SAR analysis, and the antimicrobial evaluation of 7-benzimidazol-1-yl-fluoroquinolone in in vitro, in silico, and in vivo models. Molecules 28 (16), 6018.
Millanao, A.R., et al., 2021. Biological effects of quinolones: a family of broad-spectrum antimicrobial agents. Molecules 26 (23), 7153.
Mohamed, N.G., et al., 2018. Synthesis, antimicrobial activity and molecular modeling study of 3-(5-amino-(2H)-1,2,4-triazol-3-yl]-naphthyridinones as potential DNA-gyrase inhibitors. Bioorg. Chem. 81, 599–611.
Naeem, A., et al., 2016. The current case of quinolones: synthetic approaches and antibacterial activity. Molecules 21 (4), 268.
Ndarawit W, W., et al., 2024. Discovery of α-amylase and α-glucosidase dual inhibitors from NPASS database for management of type 2 Diabetes Mellitus: a chemoinformatic approach. PLoS One 19 (11), e0313758.
Nguyen, P.T.V., et al., 2021. 2D-quantitative structure–activity relationships model using PLS method for anti-malarial activities of anti-haemozoin compounds. Malar. J. 20 (1), 264.
O'Toole, G.A., 2011. Microtiter dish biofilm formation assay. J. Vis. Exp. (47), 2437.
Opoku-Temeng, C., Sintim, H.O., 2017. Targeting c-di-GMP signaling, biofilm formation, and bacterial motility with small molecules. Methods Mol. Biol. 1657, 419–430.
Özsan, Ç., et al., 2026. A platinum butterfly effect: small changes turn an anticancer drug into a non-toxic metalloantibiotic with in vivo efficacy. NPJ Antimicrob. Resist. 4 (1), 37.
Pai, K.N., Bhat, K.S., 2026. An overview on synthetic aspects and biological activity profiles of hydrazone derivatives. Discover Chem. 3 (1), 11.
Panigrahi, S.D., et al., 2024. Enhancing antibacterial efficacy through macrocyclic host complexation of fluoroquinolone antibiotics for overcoming resistance. Sci. Rep. 14 (1), 24637.
Pham, T.D.M., et al., 2019. Quinolone antibiotics. MedChemComm 10 (10), 1719–1739.
Qayed, W.S., et al., 2022. Novel azine linked hybrids of 2-indolinone and thiazolodinone scaffolds as CDK2 inhibitors with potential anticancer activity: in silico design, synthesis, biological, molecular dynamics and binding free energy studies. Bioorg. Chem. 126, 105884.
Raies, A.B., Bajic, V.B., 2016. In silico toxicology: computational methods for the prediction of chemical toxicity. Wiley Interdiscip. Rev.:Comput. Mol. Sci. 6 (2), 147–172.
Saeloh, D., et al., 2017. Effects of rhodomyrtone on gram-positive bacterial tubulin homologue FtsZ. PeerJ 5, e2962.
Schäfer, A.B., et al., 2024. Dissecting antibiotic effects on the cell envelope using bacterial cytological profiling: a phenotypic analysis starter kit. Microbiol. Spectr. 12 (3), e0327523.
Shi, W.-K., et al., 2016. 3-Arylpropionylhydroxamic acid derivatives as Helicobacter pylori urease inhibitors: synthesis, molecular docking and biological evaluation. Bioorg. Med. Chem. 24 (19), 4519–4527.
Singh, S., et al., 2015. Quinoline and quinolones: promising scaffolds for future antimycobacterial agents. J. Enzyme Inhib. Med. Chem. 30 (3), 492–504.
Strahl, H., et al., 2014. The actin homologue MreB organizes the bacterial cell membrane. Nat. Commun. 5, 3442.
Strahl, H., Hamoen, L.W., 2010. Membrane potential is important for bacterial cell division. Proc. Natl. Acad. Sci. U.S.A. 107 (27), 12281–12286.
Struga, M., et al., 2023. N-acylated ciprofloxacin derivatives: synthesis and in vitro biological evaluation as antibacterial and anticancer agents. ACS Omega 8 (21), 18663–18684.
Tzollas, N.M., et al., 2010. A new approach to indophenol blue method for determination of ammonium in geothermal waters with high mineral content. Int. J. Environ. Anal. Chem. 90 (2), 115–126.
Vestby, L.K., et al., 2020. Bacterial biofilm and its role in the pathogenesis of disease. Antibiotics 9 (2), 59.
Wang, Y., et al., 2012. Design, synthesis and evaluation of clinafloxacin triazole hybrids as a new type of antibacterial and antifungal agents. Bioorg. Med. Chem. Lett. 22 (17), 5363–5366.
Wenzel, M., et al., 2018. The multifaceted antibacterial mechanisms of the pioneering peptide antibiotics tyrocidine and gramicidin S. mBio 9 (5), e00802–e00818.
Yanat, B., et al., 2017. Plasmid-mediated quinolone resistance in Enterobacteriaceae: a systematic review with a focus on Mediterranean countries. Eur. J. Clin. Microbiol. Infect. Dis. 36 (3), 421–435.